Linköping Studies in Science and Technology
Dissertation No. 2347

Multi-frequency SFDI: depth-resolved scattering models of wound healing

Luigi Belcastro

LINKÖPING UNIVERSITY

Linköping Studies in Science and Technology
Dissertations, No. 2347

Multi-frequency SFDI: depth-resolved scattering models of wound healing

Luigi Belcastro

Linköping University
Department of Biomedical Engineering
SE-581 83 Linköping, Sweden

Linköping 2023

Edition 1.0

ISBN 978-91-8075-355-5 (print)
ISBN 978-91-8075-356-2 (PDF)
ISSN 0345-7524
URL doi.org/10.3384/9789180753562

Typeset using LaTeX

Printed by LiU-Tryck, Linköping 2023

愛がなければ、見えない

POPULÄRVETENSKAPLIG SAMMANFATTNING

Med optiska tekniker avser vi en grupp metoder som använder ljus för att utföra mätningar. Spatial frequency domain imaging (SFDI) är en optisk teknik som fungerar genom att belysa målet med sinusformade ljusmönster och analysera den mängd som reflekteras tillbaka beroende på den spatiala frekvensen (f_x) hos mönstren. Denna frekvensspecifika respons kan användas för att bestämma materialets inneboende optiska egenskaper, t.ex. absorptionskoefficienten (μ_a) och den reducerade spridningskoefficienten (μ_s'). I biologiska tillämpningar kan dessa optiska egenskaper korreleras till fysiologiska strukturer och molekyler, vilket ger forskare och kliniker ett användbart verktyg för att studera de fenomen som sker i biologisk vävnad. Målet med detta arbete är att bidra till utvecklingen av SFDI, så att tekniken kan användas som ett diagnostiskt verktyg för att studera sårläkningsprocessen i vävnad. I artikel I introducerar vi begreppet korskanaler, som ges av den spektrala överlappningen mellan de bredbandiga LED-lamporna och RGB-kamerasensorerna som används i SFDI-instrumentationen. Syftet med korskanaler är att förbättra den begränsade spektrala informationen hos RGB-enheter, vilket gör det möjligt att detektera fler biologiska molekyler. En av de största begränsningarna med SFDI är att den bygger på antagandet att ljus sprids genom ett homogent, tjockt materialskikt. Detta antagande förlorar sin giltighet när vi vill undersöka biologisk vävnad, som består av flera tunna lager med olika egenskaper. I artikel IV har vi utvecklat en ny metod för att bearbeta SFDI-data som vi kallar multifrekvens-SFDI. I denna nya metod utnyttjar vi ljusmönstrens olika penetrationsdjup beroende på deras f_x för att få djupkänsliga mätningar. Vi definierade också en 2-lagersmodell för ljusspridning som imiterar fysiologin i ett sår, för att beräkna de partiella volymbidragen till μ_s' för de enskilda lagren. Tvåskiktsmodellen baseras på analytiska formuleringar av ljusflödet. Vi jämförde prestandan hos tre fluensmodeller, varav en har tagits fram av oss själva som en förbättring av en befintlig formulering. I artikel II kunde vi testa vår nya SFDI-metod med flera frekvenser genom att delta i en djurstudie om stamcellsbaserade regenerativa terapier. Vi bidrog genom att utföra SFDI-mätningar på läkande sår, i syfte att tillhandahålla ytterligare ett utvärderingsmått som kompletterade den kliniska utvärderingen och cellhistologin som utfördes i studien. Analysen av SFDI-data vid olika f_x belyste olika processer som sker på ytan jämfört med i den djupare vävnaden. I artikel V förfinar vi ytterligare den teknik som introducerades i artikel IV genom att utveckla en algoritm för inverslösning för att isolera tjockleken på det tunna skiktet och de skiktspecifika μ_s'. De rekonstruerade parametrarna testades både på tunna optiska silikonfantomer och ex-vivo brännskador som behandlats med stamceller.

ABSTRACT

With optical techniques, we refer to a group of methods that use of light to perform measurements on matter. Spatial frequency domain imaging (SFDI) is an optical technique that operates in the spatial frequency domain. The technique involves using sinusoidal patterns of light for illumination, to study the reflectance of the target based on the spatial frequency (f_x) of the patterns. By analysing the frequency-specific response with the aid of light transport models, we are able to determine the intrinsic optical properties of the material, such as the absorption coefficient (μ_a) and reduced scattering coefficient (μ_s') In biological applications, these optical properties can be correlated to physiological structures and molecules, providing a useful tool for researchers and clinicians alike in understanding the phenomena happening in biological tissue. The objective of this work is to contribute to the development of SFDI, so that the technique can be used as a diagnostic tool to study the process of wound healing in tissue. In paper I we introduce the concept of cross-channels, given by the spectral overlap of the broadband LED light sources and the RGB camera sensors used in the SFDI instrumentation. The purpose of cross-channels is to improve the limited spectral information of RGB devices, allowing to detect a larger number of biological molecules. One of the biggest limitations of SFDI is that it works on the assumption of light diffusing through a homogeneous, thick layer of material. This assumption loses validity when we want to examine biological tissue, which comprises multiple thin layers with different properties. In paper IV we have developed a new method to process SFDI data that we call multi-frequency SFDI. In this new approach, we make use of the different penetration depth of the light patterns depending on their f_x to obtain depth-sensitive measurements. We also defined a 2-layer model of light scattering that imitates the physiology of a wound, to calculate the partial volume contributions to μ_s' of the single layers. The 2-layer model is based on analytical formulations of light fluence. We compared the performance of three fluence models, one of which we have derived ourselves as an improvement over an existing formulation. In paper II we were able to test our new multi-frequency SFDI method by participating in an animal study on stem-cells based regenerative therapies. We contributed by performing SFDI measurements on healing wounds, in order to provide an additional evaluation metric that complemented the clinical evaluation and cell histology performed in the study. The analysis of the SFDI data at different f_x highlighted different processes happening on the surface compared to the deeper tissue. In paper V we further refine the technique introduced in paper IV by developing an inverse solver algorithm to isolate the thickness of the thin layer and the layer-specific μ_s'. The reconstructed parameters were tested both on thin silicone optical phantoms and ex-vivo burn wounds treated with stem cells.

Acknowledgments

This is probably the most difficult part of the entire book. I am sitting here, thinking about the five years journey that brought me to this point and all the people that one way or another had an influence on my life. It's impossible for me to remember everything that happened in such a long period, so there will probably be omissions, but I want to ensure you they are not due to malice on my part.

First, I want to give thanks to my supervisor Rolf for believing in me until the end. To all the colleagues and students that came to work in our lab and the ones who left, for the help, support and fun afterwork activities. To the people at IMT for the coffee breaks and complaining about life as a PhD student.

I want to thank all the people I met through Forum Scientium for the opportunities and social events. In particular to Stefan, who I hope is enjoying retirement, and Rozalyn, who is doing a good job at steering the ship.

A special thanks goes to prof. Keiichiro Kagawa and all the staff at Shizuoka University, who made my dream of traveling to Japan a reality.

In no particular order, thanks to the *Amigos* for the cooking workshops and outing activities, to the *Sweet Chickpeas* for the dinners and the festive mood, to *Baffarbaffo's Party* for the (somewhat) weekly game sessions, to George and Ellen for the long awaited (albeit short lived) TTRPG campaign, to the *Grifoni del Mercoledì* for being the same group of crazy people I left in Turin five years ago. You all helped me feel less alone while living in a new country.

Finally, I thank the people that are a constant presence in my life. Elisa, who has been tolerating me for more than six years and is the reason I ended up in Sweden. Dora and Vega, who have been helping me keep my sanity, one cat nap at a time. My parents and a long list of relatives, who I don't see very often but still complain and worry about me like I was 10 years old. My sister, who is busy enjoying youth and finding her path in life.

To conclude this section, I think this xkcd.com comic included in the thesis template is very fitting, so I will just leave it in the next page. To the committee members taking part in my defense: do not worry, in Sweden is (sadly) not custom to give out graduation swords to PhD candidates.


IN CONCLUSION,
AAAAAAAAAAAA!!!
THE BEST THESIS DEFENSE IS A GOOD THESIS OFFENSE.

Contents

List of Papers

This thesis is based on the following publications, referred to in the text with their roman numeral:

I. L. Belcastro, H. Jonasson, T. Strömberg, and R. B. Saager
Handheld multispectral imager for quantitative skin assessment in low-resource settings
Journal of Biomedical Optics, vol. 25, no. 08, p. 1, Aug. 2020
DOI: 10.1117/1.jbo.25.8.082702, LiU repository number: diva2:1469708

II. Hady Shahin, Luigi Belcastro, Jyotirmoy Das, Marina Perdiki Grigoriadi, Rolf B Saager, Ingrid Steinvall, Folke Sjöberg, Pia Olofsson, Moustafa Elmasry and Ahmed T El-Serafi
miR-155 mediates multiple gene regulations pertinent to the role of human adipose-derived mesenchymal stem cells in skin repair
Manuscript submitted to Advances in Wound Care

III. L. Belcastro, H. Jonasson, T. Strömberg, A. Elserafy, R. Saager Luigi Belcastro, and R. B. Saager
Beneath the skin: multi-frequency SFDI to detect thin layers of skin using light scattering
Proceedings Volume 12352, Photonics in Dermatology and Plastic Surgery 2023, pp. 44–48
DOI: 10.1117/12.2648545, LiU repository number: diva2:1792365

IV. Luigi Belcastro, Hanna Jonasson, Rolf B Saager
Multi-frequency SFDI: a depth-resolved optical scattering model to isolate scattering contrast in thin layers of skin
Manuscript under review at Journal of Biomedical Optics

V. Luigi Belcastro, Hady Shahin, Moustafa Elmasry, Ahmed T El-Serafi, Hanna Jonasson, Rolf B Saager
Multi-frequency SFDI: inverse solving algorithm to reconstruct depth-resolved scattering properties in wound healing
Manuscript submitted to the Journal of Biomedical Optics

List of Figures

Abbreviations

The following is a list of the abbreviations and symbols appearing in this thesis.

δ	Penetration depth
ε	Extinction coefficient
f_x	Spatial frequency (in the x direction)
g	Anisotropy factor
λ	Light wavelength
μ_a	Absorption coefficient
μ_s	Scattering coefficient
μ_t	Transport coefficient
μ_s'	Reduced scattering coefficient
μ_{eff}	Effective scattering coefficient
n	Refraction index
$p(\theta)$	Phase function
ϕ	Fluence rate
σ_s	Scattering cross-section
τ	Optical depth / optical thickness
Al_2O_3	Aluminium dioxide
DNIRS	Diffuse near infrared spectroscopy
ECM	Extracellular matrix
EM	Electromagnetic
Hb	Haemoglobin
HbO	Oxygenated haemoglobin
HT	Hankel transform
IR	Infrared
LSI	Laser speckle imaging
M_{AC}	Modulated intensity
MC	Monte Carlo
NIR	Near infrared
OCT	Optical coherence tomography

PDMS	Polydimethylsiloxane (Silicone)
PHD	Photon hitting density
R_d	Diffuse reflectance
RMSE	Root mean square error
RTE	Radiative transport equation
SDA	Standard diffusion approximation
SFD	Spatial frequency domain
SFDI	Spatial frequency domain imaging
SFDS	Spatial frequency domain spectroscopy
TiO_2	Titanium dioxide
UV	Ultraviolet
WHR	Wound healing rate

1

Introduction

A wound is a disruption of biological tissue that compromises its functionality. When a tissue is wounded, the body will undergo a long process of healing, that involves different biological components acting on different time scales [1, 2, 3]. There are four phases in the healing process: hemostasis, inflammation, proliferation and remodeling, which can last anywhere from a few hours to a few months. When a wound is not following the normal healing process, we are in the presence of a *chronic wound* or non-healing wound. A chronic wound can be caused both by external factors (e.g. bacterial infection) or preexisting internal conditions. Chronic wounds comport high management costs and can bring complications leading to reduction in the quality of life and higher mortality rates [4]. For this reason, early detection of irregularities in the healing process is essential so that corrective measures can be taken to avoid the formation of non-healing wounds.

In order to assess the progression of healing, multiple techniques are required to measure parameters for all these factors involved at different stages. The assessment methods can range from simple and non-invasive (e.g. visual inspection) to highly specific and disruptive (e.g. biopsy and cell histology).

Optical methods present ideal characteristics that makes them a potentially valuable addition to the tools available to the healthcare personal for the assessment of wounds. Optical methods are techniques that use light to perform measurements that can be related to specific biological phenomena. They have the advantages of being non-invasive, fast and able to detect microscopical features on a large area. Optical devices can also be compact and low-cost, making their integration in clinical and remote medical setting easy. The optical method we use is called Spatial Frequency Domain Imaging (SFDI), which works by projecting sinusoidal patterns of light on the tissue and measuring the frequency-dependent tissue diffuse reflectance ($R_d(f_x)$).

Scattering is a useful source of information in biological tissue that can be correlated with the dimension and density of microscopical organelles and extracellular matrix (ECM) components. In wound healing assessment applications, light scattering can be used to differentiate between different tissues associated with different phases of healing (e.g. collagen formation, re-epithelization...). Most optical methods work under the assumption of homogeneous tissue, which is not really suited to wound healing applications, as the process involves heterogeneous tissue at various depths. For this purpose, we introduce a new approach to process data obtained from SFDI

called *multi-frequency SFDI*, which adds depth information to the measurements of optical properties. The increased sensitivity in depth is then used as a basis to develop a 2-layer model of light scattering, which can isolate layer-specific optical properties related to the different mechanisms of a healing wound. The model is used to extract optical parameters from the multi-frequency SFDI data, that are useful for wound assessment purposes.

1.1 Aim

The aim of this thesis is to improve the SFDI technique for the purpose of studying skin conditions, providing tools that can be useful for diagnosis in a clinical setting. The techniques and models developed in this work are focused in particular on the assessment of wound healing through light scattering. In particular the aim is to:

1. Develop customized SFDI systems tailored for the applications in the study, with an emphasis on ease of use and portability to be able to acquire data in a variety of research and clinical settings.
2. Develop and test models of light transport to process SFDI data and extract depth-specific scattering properties, which will be used as biological indicators in the assessment of wound healing.

1.2 Structure of the thesis

Chapter 2 gives a background on the subject of the application, nominally skin physiology, wounds and the healing process, light interactions with tissue and optical properties. Chapter 3 describes the principles of SFDI, the instrumentation necessary and how the data is processed. This chapter also explores multiple models of light transport used in SFDI data processing. Finally, the concept of multi-frequency SFDI is introduced. Chapter 4 is about tissue-simulating optical phantoms, what are their applications and how are they manufactured. This chapter also explores how these tissue simulating phantoms can be used as stable, traceable references and standards to test and evaluate the performance of new optical methods. Chapter 5 introduces a 2-layer scattering model, what are its governing equations and how an inverse solving algorithm is used to extract parameters from multi-frequency SFDI measurements.

2

Background

2.1 Skin physiology

The skin is the largest organ in the human body and it acts as a physical barrier and interface to the external world. It is made up by several layers of tissues and cells, which can be roughly categorized in three principal layers: the epidermis, the dermis and the hypodermis (shown in figure 2.1) [5].

The *epidermis* is the most superficial skin layer. It varies in thickness around the body, from approximately $100\mu m$ to 1mm in the thickest regions (e.g. the soles of the feet). It is itself organized in multiple layers of epithelial cells and it presents no blood vessels. Most of the cells in the epidermis are *keratinocytes*, cells that produce the keratin protein, which is what makes the skin, hair and nails rigid and waterproof. Cells on the surface of the epidermis are constantly dying and being replaced by new cells born from epidermal stem cells in the deeper layers. This means that we are literally wearing an entire new skin approximately every two months [6]. Another important component found on the deeper layer of the epidermis are the *melanocytes*, cells responsible for the production of melanin as a protective measure when the skin is exposed to UV rays.

Below the epidermis we find the *dermis*, a layer made up mostly by connective tissue with a thickness ranging around 1-4mm. The dermis contains other tissues such as blood vessels, nerves, sweat glands and hair follicles. It can be divided in two layers: the *papillary layer*, made up by loose collagen and elastin fibres generated by fibroblasts cells, and the *reticular layer*, a more dense and irregular layer of connective tissue, rich in blood vessels and nerve endings.

The deepest layer of the skin is the *hypodermis*, or subcutaneous layer. It is the thickest layer, ranging from few millimeters up to 3 centimeters. Its main functions are to connect the skin to the muscle and bone underneath and to store fat tissue, both for insulation and energy storage purposes.

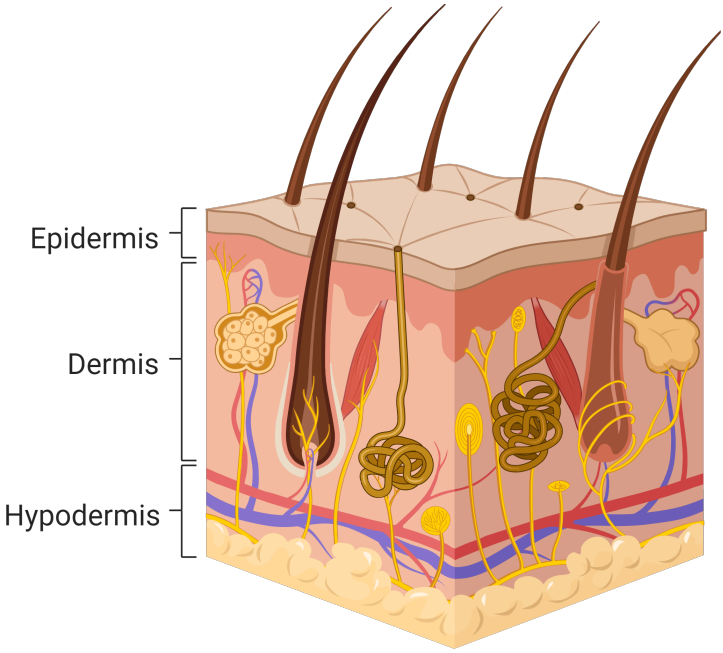

Figure 2.1: The three layers of the skin and the tissues they contain. Figure made with Biorender.com

Wounds and healing

Being the organ most exposed to the environment, the skin is also particularly subject to damage. When the ability of the skin to act as a barrier is compromised, the body is left vulnerable to water loss, infections and thermal imbalance. Wounds can caused by a multitude of factors, that can either be internal (like diabetic ulcers) or external (like burns, abrasions and lacerations) [7]. Wounds can also be classified depending on their severity:

- **superficial**: when the wound is limited to the epidermis.
- **partial thickness**: when the wound extends to part of the dermis.
- **full thickness**: when there is a complete loss of dermis and the wound extends to the sub-dermal tissues.

The healing process is continuous, but four general phases can be distinguished. The first phase is *hemostasis*, which begins right after the wound formation and involves contraction of the blood vessels and coagulation to stop any bleeding. The coagulated blood also serves as a support for the migration of cells in the following phases.
The second phase is *inflammation*, in which cytokines are released in the hours following the wound formation to increase the production of white blood cells and combat external pathogens. An over-expression of cytokines can bring to the destruction of the new formed tissue, and is one of the causes of chronic wounds.

In the following days, the migration of fibroblasts in the wound site gives start to the third phase, *proliferation*, that is characterized by production of collagen type III to form a semi-permanent ECM which causes the wound to contract, and migration of epithelial cells from the wound edges (i.e. re-epithelization). At the same time, angiogenesis is promoted by growth factors to bring oxygen to the new cells, through the formation of a new micro-circulatory network.
The final phase, *remodeling*, can last months to years and consists in the replacement of the collagen type III with collagen type I, in order to form a more permanent ECM and scar tissue. The new collagen might regain up to 80% of the original tensile strength of the healthy tissue.

Wound assessment methods

In literature, it's possible to find a great quantity of methodologies for wound assessment, ranging from standard visual inspection to histopatological analysis and imaging techniques [3]. This section gives an overview of the methods currently used in clinical practice and what parameters are they measuring.

Wound Healing Rate (WHR): It's the most reliable measurement that can be done in clinical practice. The WHR is defined as the percentage change in wound area: $WHR = (A_i - A_f)/A_i$, where A_i is the initial wound area and A_f the final area [3].

Here follows a list of the most common assessment techniques currently in use:

- **Wound tracing**: it's an inexpensive way of tracking the shape and dimension of a wound over time. Its done by placing a transparent film over the wound and tracing the margins with a marker.
- **Photography**: it's a non-invasive method useful for documenting the evolution of wounds, capable of capturing both the shape, dimension and color. A few things need to be considered when taking a picture, to avoid altering the perspective or the color of the wound. A scale should also always be present for size reference (e.g. a ruler). Analysis of digital pictures can be easily performed by software, either manually or automatically.
- **Histopatological analysis**: it's an invasive method that requires a biopsy on the wound, but it's useful to understand better the physiology of non-healing wounds (watching for structural changes, looking for malignancies...). The tissue from biopsy is subject to several processes like freezing, sectioning and staining. Colored dyes are used to highlight the features most relevant in wound healing (white blood cells, blood vessels, collagen, cell nuclei, fibroblasts...).
- **Immunoassay**: it's a group of techniques that use antibodies to detect specific molecules. In the context of wound healing, immunological techniques can be used to quantify the presence of cytokines and growth factors.
- **Biochemical methods**: it's a large category of techniques used to detect the presence of proteins and other biological molecules associated with some as-

pect of wound healing. Examples include *hydroxyproline* for detecting collagen, *myeloperoxidase* to detect neutrophils and *reactive oxygen species* to determine if the cells are suffering from oxidative stress.

- **Optical methods**: a category of non-contact, non-invasive measurements techniques using light. Common methods used on tissue include optical coherence tomography (OCT) to study microscopic morphological changes, diffuse near-infrared spectroscopy (DNIRS) to quantify the level of oxygenated and de-oxygenated haemoglobin, and laser speckle imaging (LSI) to assess the microcirculation.

2.2 Light interaction with tissue

Light is an electromagnetic radiation, which occupies just a small portion of the electromagnetic (EM) spectrum. There are different definitions of what ranges of the EM spectrum are considered "light" depending on the application [8], so for the sake of clarity the definition used in the field of biophotonics will be adopted (shown in figure 2.2). This definition is based on the principal types of interaction of light with biological tissue and spans the range of wavelengths (λ) from 100nm to 1000μm. This interval is further classified in spectral ranges: *ultraviolet* (UV) light: 100nm - 400nm; *visible* light: 400nm - 780nm; *infrared* (IR) light: 780nm - 1000μm. In biomedical applications is also useful to specify a *near infrared* (NIR) range that includes light in the spectrum 780nm - 2500nm.

In a vacuum, light travels in a straight line at a constant speed of $c = 3 \cdot 10^8 \text{m/s}$. When a light beam enters a different a material, its speed and direction are modified according to Snell's Law:

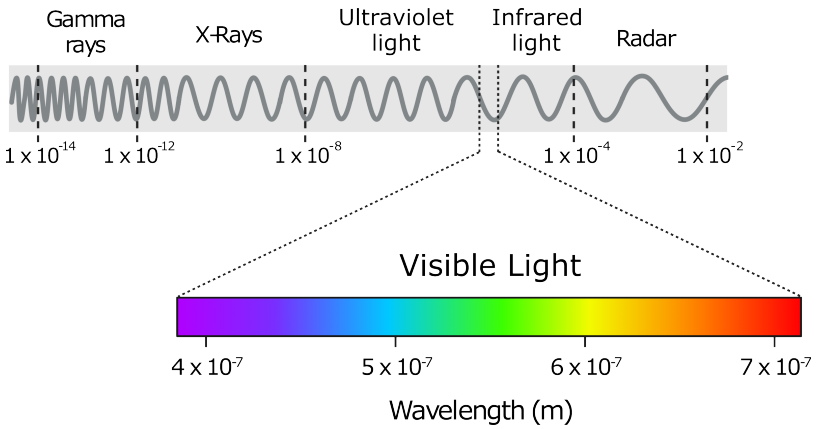

Figure 2.2: The electromagnetic spectrum with respective wavelengths. Image made with Biorender.com

$$\frac{\sin\theta_1}{\sin\theta_2} = \frac{n_1}{n_2} = \frac{v_1}{v_2} \tag{2.1}$$

Where θ is the angle of incidence with respect to the normal to the incident surface, n_1, n_2 are the refractive indices of the two materials and v_1, v_2 are the velocities of light in the medium. Vacuum (and by approximation, air) has by definition $n = 1$ and $v = c$. In biological tissue n can range approximately between 1.37 - 1.45, but for skin is commonly assumed $n = 1.4$.

This equation is actually a simplification that is valid only for homogeneous, non-scattering media with a smooth surface. Most of biological tissues are instead turbid, non-homogeneous and rough, so the propagation of light is non-ideal and complicated by the insurgence of other phenomena. The following sections are going to illustrate the most common tissue-light interaction that are of interest in the biomedical field.

Absorption

Absorption happens when light loses part of its radiating energy while traversing a material. Absorption in tissue is mainly due to the presence of *chromophores*, molecules that have the capacity of absorbing light at certain wavelengths by transferring the photons' radiation energy to their molecules (e.g. electron transition, vibration modes, rotation modes...). The level of radiation energy depends on the wavelength of light, which then determines what is the principal phenomena involved. For example light in the UV-visible spectrum is mainly transferred to electronic excitation, while light in the IR spectrum causes molecule vibrations.
Absorption in tissue is represented by the *absorption coefficient* (μ_a), which indicates on average what is the probability of a photon to be absorbed per unit length and is usually measured in cm^{-1} or mm^{-1}. The absorption coefficient is directly related to the characteristic extinction coefficient (ε) of the chromophore and its molar concentration (C) [9]:

$$\mu_a = C\varepsilon \tag{2.2}$$

Or when more than one chromophore is present:

$$\mu_a = \sum_i C_i \varepsilon_i \tag{2.3}$$

A simple equation that models the behavior of light absorption is Lambert-Beer's law:

$$I(d) = I_0\, exp(-\mu_a \cdot d) \tag{2.4}$$

Where I_0 is the incident light intensity and d is the distance travelled by light. Lambert-Beer's law is based on the assumptions that the incident light is monochromatic, absorption is limited to a single direction and the absorbers are independent from each other. Lambert-Beer is also only valid where absorption is the only source of light attenuation. In turbid media the problem becomes more complex as the presence of scattering randomly alters the propagation direction, so that each photon will travel along a different path of unknown length.

Some of the principal absorbers found in biological tissue are described in the following section, and their absorption spectra are shown in figure 2.3, which shows their unique absorbing features [9].

- **Haemoglobin**: a molecule present in red blood cells, which is responsible of binding to oxygen (O_2) and carbon dioxide (CO_2) molecules. This is made possible by a protein complex called *heme group* containing an iron atom which gives the cells their characteristic red color. Haemoglobin can be normally found in two states: oxygenated (HbO) and de-oxygenated (Hb), each of which has a characteristic absorption spectrum. Met-haemoglobin (Met-Hb) is a product of haemoglobin degradation that can be found in coagulated blood and wounds.
- **Bilirubin**: an haemoglobin metabolic byproduct with a typical yellow color, produced from the breakdown of old red blood cells and processed by the liver. An abundance of bilirubin can give a skin a yellow tint (*jaundice*) and may be a sign of problems with the liver.
- **Melanin**: a molecule produced in the epidermis as a protection against UV light. There are two main types of melanin present in skin: *eumelanin*, characterized by a brown tint, and *pheomelanin*, with a typical red tint.
- **Carotenoids**: it's a category of similar molecules (beta carotene, licopene...) that possess an orange tint and can be found in fruits and vegetables. They are converted in vitamin A in the body and are lipid soluble, so they accumulate in fat tissue (e.g. liver, subcutaneous fat).
- **"Transparent" molecules**: Not all substances found in the body have an absorption spectrum in the visible light range. For example *water* and *lipids* do not have molecular structures that allow them to transfer photon energy in the visible spectrum to their electrons, but instead they have significant vibrational modes, which causes high absorption in the NIR spectrum.

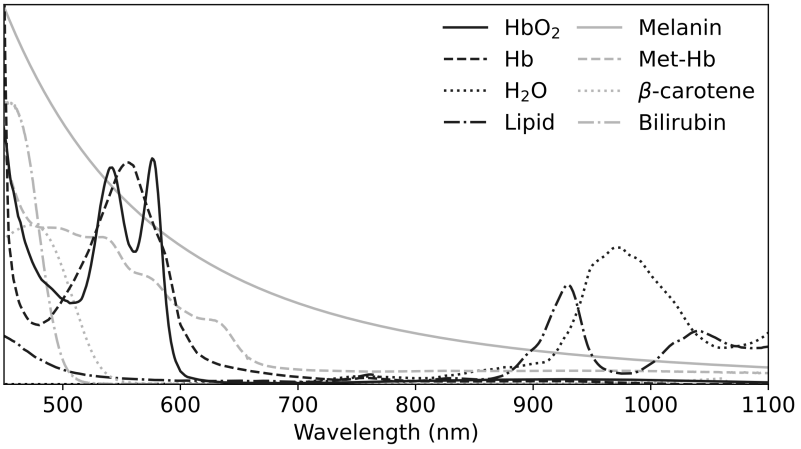

Figure 2.3: Absorption spectra of the principal chromophores in biological tissue. The curves are represented with an arbitrary scale on the vertical axis.

Scattering

Scattering happens when light encounters an obstacle on a microscopic scale, with a different refractive index (n) from the one it's currently traversing. There is no loss of energy, but the direction of the photon is altered. The distribution of the scattering particles in turbid media is considered to be random, so scattering is a stochastic phenomenon. Typical models assume the scattering particles to be spherical, which allows to model it exactly according to Mie theory (if the size of the particles is comparable or larger than λ), or Rayleigh theory (when the size of the particles is much smaller than λ) [10]. When the obstacle is much larger than λ, then the behaviour of light can be simply modeled through Snell's Law (equation 2.1).
In tissue, bulk scattering is represented by the scattering coefficient (μ_s), which is given by the scattering cross-section (σ_s) and the density of the scattering particles per unit volume (N_s).

$$\mu_s = \sigma_s N_s \tag{2.5}$$

The scattering cross-section is the probability of light scattering given by a single particle, and it is not exactly equal to the particle cross-section (A_s), but it is closely related to it by a coefficient called scattering efficiency (Q_s).

$$\mu_s = \sigma_s N = Q_s A_s N_s \tag{2.6}$$

The scattering coefficient is dependent on the wavelength of light and can be modelled with a relation of the kind: $A\lambda^{-b}$, for Mie scattering or $A\lambda^{-4}$ for Rayleigh scattering, where the coefficient b is in the range (0 - 4). Some models include contributions from both Mie and Rayleigh scattering:

$$\mu_s(\lambda) = A_1\lambda^{-b} + A_2\lambda^{-4} \tag{2.7}$$

The coefficient A is the **scattering amplitude**, which is a dimensionless quantity related to the density of scattering particles. The coefficient b is the **scattering slope**

which is related to the size distribution of the particles in the tissue [11, 12]. Examples of biological scatterers in tissue (and their order of magnitude) include: cell membranes (10nm), collagen fibrils (50 - 500nm), mitochondria (1μm) and cells (10μm).

Anisotropy factor

The scattering coefficient can tell what is likelihood of scattering in a tissue, but it tells nothing about the direction changes. This is modeled by the *scattering phase function* $p(\theta)$, which represents the probability distribution for a photon to be scattered at an angle θ with respect to the incident direction. The phase function is normalized so that the integral of $p(\theta)$ over the solid angle is equal to 1.
The phase function is a property specific to a single scattering particle, depending on its size and shape, so it is unsuited to represent the bulk property of the tissue. A more appropriate coefficient is the *anisotropy factor* (g), which is defined as the average cosine of the scattering angle, obtained by integrating the phase function over the entire solid angle (Ω):

$$g = \langle \cos\theta \rangle = \int_{4\pi} \cos\theta \; p(\theta) \; d\Omega \tag{2.8}$$

If the light is unpolarized and the particles isotropic, there is no dependence on the azimuthal angle (φ), which is assumed to have an equal probability of scattering in any direction, and the equation can be expressed as a function of the angle θ:

$$g = \langle \cos\theta \rangle = 2\pi \int_0^{2\pi} \cos\theta \; p(\theta) \; \sin\theta \; d\theta \tag{2.9}$$

The value of g is normalized between 0 and 1. For very small values of g, approaching zero, the scattering is caused by particles much smaller than λ and is almost completely isotropic. In the opposite extreme, for values of g approaching 1, the scattering particles are much larger than λ and the scattering is extremely forward-directed. Biological tissue has different distributions of particles of different sizes, so typical values of g range between 0.75 - 0.98 [13].

Reduced scattering coefficient: since in tissue the scattering events are primarily forward directed (small angular deviation), it is convenient to define a reduced scattering coefficient

$$\mu_s' = (1 - g)\mu_s \tag{2.10}$$

μ_s' is correlated to the probability of encountering an isotropic scattering event (major angular deviation). The relation in equation 2.10 is a *similarity relation*, because different combinations of g and μ_s exist that can return the same μ_s' value. This consideration, however is only valid for large source-detector separations. When dealing with small optical distances (in a regime called *sub-diffuse*), higher order approximations of anisotropy give a better representation of light scattering [14, 15].

Fluorescence

Fluorescence is a secondary phenomenon that can happen after light absorption. The photon energy excites molecules to a high energy state, which then decays to the ground energy state by emitting a photon. Some of the energy is lost in the process, so the emitted photon has a longer wavelength than the absorbed one, a phenomenon called *red-shift*. The emission is not instantaneous, since it involves thermal relaxation of molecules. The time τ between the excitation and re-emission is the *fluorescence halftime*, which in biological tissue is on the order of nanoseconds. Fluorescence is a tool widely used in biochemistry, as a non-invasive method to identify the presence of molecules and their concentration.

Phosphorescence: it's a particular type of fluorescence, where the energy decay is very slow (from milliseconds to seconds). This usually happens when the transition from the excited state to the ground state of the molecule is "forbidden" according to quantum mechanics, so the molecule is held in the excited state longer because the decay is thermodynamically unfavourable. Phosphorescence is at the base of biological phenomena like bioluminescence.

3

SFDI

Spatial frequency domain imaging (SFDI) is an optical method and the subject of this thesis. SFDI measures the *diffuse reflectance* (R_d), which is the non-specular light that is reflected back from the tissue, using sinusoidal patterns of light. By changing the spatial frequency (f_x) of these patterns, the response of the tissue changes depending on the combination of absorption (μ_a) and reduced scattering (μ_s') of the tissue [16]. In particular, measurements at low f_x are more sensitive to variations in absorption, while measurements at higher f_x are more sensitive to variations in scattering. By modeling this behaviour of $R_d(f_x, \mu_a, \mu_s')$, it is possible to reverse the solution, starting from experimental measurements of the diffuse reflectance, and obtain the (μ_a, μ_s') of the tissue, as will be further explained in section 3.1. The problem is generally not easy, as a reverse solution might not correspond to an unique combination of (μ_a, μ_s'). This process usually involves one of two approaches:

- The use of a pre-computed lookup table of $R_d(f_x)$ for every possible combination of (f_x, μ_a, μ_s'), which is a fast but less accurate method.
- An optimization approach, where the measured $R_d(f_x)$ is compared with a model (either analytical or numerical simulation) and the parameters (μ_a, μ_s') are iteratively updated in the parameter space in search of a global solution.

This chapter will describe the principles upon which SFDI is based, the necessary instrumentation and how the data is acquired and processed. The chapter ends by introducing *multi-frequency SFDI*, which is the new approach to processing SFDI data at the core of this thesis work.

3.1 Principles

Radiative Transport Equation

In order to understand how SFDI is used to measure the optical properties of a material, it's necessary to understand how light propagates and is influenced by μ_a and μ_s'. The *radiative transport equation* (RTE) is the equation at the base of everything and

it describes how light propagates in a turbid medium, like biological tissue [17]:

$$\frac{1}{v}\frac{\partial L(r,\Omega,t)}{\partial t} + \Omega \cdot \nabla L(r,\Omega,t) = \\ -\mu_t L(r,\Omega,t) + \mu_s \int_{4\pi} L(r,\Omega,t) p(r,\Omega' \rightarrow \Omega) d\Omega' + Q(r,\Omega,t) \tag{3.1}$$

Following are the definitions of its components:

- v is the speed of light in the medium
- $L(r,\Omega,t)$ is the *Radiance*, the energy flow per unit of area, solid angle and time.
- Ω is the solid angle
- $\mu_t = \mu_a + \mu_s$ is the *transport coefficient*
- $p(r,\Omega' \rightarrow \Omega)$ is the *phase function*
- $Q(r,\Omega,t)$ is the volumetric source term, which includes all the other internal sources of light (e.g. fluorescence, virtual sources...).

Then a breakdown of its contributions:

- $\frac{1}{v}\frac{\partial L(r,\Omega,t)}{\partial t}$ is the variation of radiance over time.
- $\Omega \cdot \nabla L(r,\Omega,t)$ is the variation of radiance over the solid angle.
- $-\mu_t L(r,\Omega,t)$ are the losses of radiance due to absorption and scattering.
- $\mu_s \int_{4\pi} L(r,\Omega,t) p(r,\Omega' \rightarrow \Omega) d\Omega'$ is called *Green's equation* and it represents the gain of radiance due to light that is scattered from adjacent volumes.

The presence of Green's equation makes the RTE impossible to solve directly, so different approaches have been developed over time that make use of either approximations of Green's equation or numerical simulations like the Monte Carlo method. The RTE is normally solved in terms of light *fluence rate* (ϕ), which is an indication of the light power per unit area, and reflectance (R), which is a measure of the light energy reflected at the surface.

Diffusion Approximation

By using this simplification of the RTE, it is possible to reduce it to a first order differential equation, which is possible to solve. The *standard diffusion approximation* (SDA) is based on the following assumptions:

- The measured light field must be completely diffuse (distance $>> 1/\mu_s'$).
- Scattering is predominant over absorption ($\mu_s' >> \mu_a$).
- The medium is homogeneous.

In the SDA, radiance is expressed as a 1st order spherical harmonics expansion, including one isotropic fluence rate (ϕ) term and one anisotropic directional flux (J) [18]. By applying the appropriate boundary conditions and source terms, the SDA can be solved to obtain ϕ and the diffuse reflectance R_d. The full derivation of the SDA can

be found in previous works from other groups [18]. In the next section is reported the equation of ϕ (normalized to the incident power P_0) in the spatial frequency domain [16], as it is relevant to the thesis work:

$$\frac{\phi(z, f_x)}{P_0} = A \cdot \exp(-\mu_t\, z) + C \cdot \exp(-\mu'_{eff}(f_x)\, z) \tag{3.2}$$

Where $\mu_t = \mu_a + \mu'_s$, $\mu_{eff} = \sqrt{3\mu_a\mu_t}$ and $\mu'_{eff} = \sqrt{\mu^2_{eff} + (2\pi f_x)^2}$ if the patterns are 1D and oriented in the x direction. The A and C coefficients are obtained trough the appropriate boundary conditions:

$$A = \frac{3\mu'_s/\mu_t}{({\mu'_{eff}}^2/\mu_t^2) - 1}$$

$$C = \frac{-3(\mu'_s/\mu_t)(1+3R)}{\left(\frac{\mu'_{eff}}{\mu_t^2} - 1\right)\left(\frac{\mu'_{eff}}{\mu_t} + 3R\right)}$$

$$R = \frac{1 - R_{eff}}{2(1 + R_{eff})} \tag{3.3}$$

R_{eff} is the effective Fresnel coefficient and is normally obtained from a polynomial function of the refractive index (n):

$$R_{eff}(n) \approx 0.0636n + 0.668 + 0.71n^{-1} - 1.44n^{-2}$$

δ-P1 approximation

Scattering from particles presents a strong anisotropy, which is impossible to correctly represent with low order approximations. In this context, the δ-P1 approximation is an enhancement over the SDA, as it takes in account the strong asymmetrical forward scattering of the phase function [19].
The δ-P1 approximation is based on a model of the phase function $p(cos\theta)$ that includes a Dirac delta to represent the forward scattering peak and an isotropic two-term expansion of the phase function [20]:

$$p(\cos\theta) = \frac{1}{4\pi}[2f\delta(1 - \cos\theta)] + (1 - f)[1 + 3g^*(\cos\theta)] \tag{3.4}$$

Where f is the amount of light that is forward scattered and g^* is the anisotropy factor of the remaining (1-f) diffused scattered light. To obtain the values of f and g^*, the δ-P1 is set to approximate another phase function, like the Henyey-Greenstein phase function [21]. This gives as a result the following values:

$$f = g_1^2 \qquad\qquad g^* = \frac{g_1}{1 + g_1}$$

with g_1 being the first moment of the phase function obtained from the Legendre polynomial [19, 20]. The full derivation can be found in Carp et al. [20], but it should be noted that this implementation is not specific to the spatial frequency domain (SFD). An alternative version of the δ-P1 approximation for the SFD was described in Seo's doctoral thesis [22], including an AC and a DC component. The solution for

ϕ_{AC} (normalized to the incident power P_0) is reported in the following section for convenience:

$$\frac{\phi_{AC}(z, f_x)}{P_0} = \frac{C^*}{\mu'_{eff} - \mu_t^*}[\exp(-\mu_t^* z) - \exp(-\mu'_{eff} z)] + \frac{C^*}{\mu'_{eff} + \mu_t^*}[\exp(-\mu_t^* z) - \exp(-\mu'_{eff}(z + 2z_b))] \quad (3.5)$$

where $\mu_s^* = (1-f)\mu_s$, $\mu_t^* = \mu_a + \mu_s^*$ and the constants C^* and z_b are obtained by the application of boundary conditions:

$$C^* = \frac{3\mu_t \mu_s^*}{2\mu'_{eff}}; \qquad z_b = \frac{2}{3\mu_t}\frac{1+R_1}{1-R_1} \quad (3.6)$$

R_1 is the first moment of the Fresnel reflection coefficient. The ratio

$$R^* = (1+R_1)/(1-R_1)$$

is usually simplified by a polynomial function of the refractive index (n) (accurate within 1% error):

$$R^*(n) \approx -0.1375n^3 + 4.339n^2 - 4.90366n + 1.6896 \quad (3.7)$$

Modified δ-P1

An alternative δ-P1 approximation was derived in paper IV, by extending the original derivation described in Carp et al. [20] to the spatial frequency domain, with a procedure similar to what Cuccia et al. have done for the SDA [16]. This new δ-P1 approximation is called *modified δ-P1* or mod-δ-P1, and its full derivation can be found in the appendix of paper IV [23]. In the following section is the mod-δ-P1 equation for ϕ (normalized to the incident power P_0):

$$\frac{\phi(z, f_x)}{P_0} = (1 + A')\exp(-\mu_t^* z) + C' \exp(-\mu'_{eff} z) \quad (3.8)$$

With the coefficients:

$$A' = \frac{3\mu_s^*(\mu_t^* + g^*\mu_a)}{{\mu'_{eff}}^2 - {\mu_t^*}^2}$$

$$C' = \frac{-A'\left(1 + \frac{2}{3}R^*\mu_t\mu_t^*\right) + 2R^*\mu_t\, g^*\mu_s^*}{\left(1 + \frac{2}{3}R^*\mu_t\mu'_{eff}\right)}$$

$$R^* = \frac{1+R_1}{1-R_1} \quad (3.9)$$

Where $\mu_s^* = \mu_s(1-f)$, $\mu_t^* = \mu_a + \mu_s^*$, $\mu_{eff} = \sqrt{3\mu_a\mu_t}$ and $\mu'_{eff} = \sqrt{\mu_{eff}^2 + (2\pi f_x)^2}$. The Ratio of the Fresnel coefficients R* is the same already seen in equation 3.6 and can be calculated with the polynomial in equation 3.7.

Monte Carlo method

A different approach in solving the RTE is using stochastic methods of photon transport. The Monte Carlo (MC) method is a class of algorithms that are used to solve problems dealing with uncertainty by repeatedly doing random sampling and obtaining a numerical solution. In order for the Monte Carlo method to be reliable, the quantity of random samples must be large enough to satisfy the law of large numbers [24]. Monte Carlo methods are more accurate than analytical solutions like SDA and $\delta-$P1 for certain aspects, like in proximity of boundaries and in regimes where the diffusion assumptions are not valid (e.g. when μ_a is comparable to μ_s'). On the other hand, it is a much slower approach and it requires significantly higher computing power.
A MC algorithm for photon transport follows this general routine, repeated for a large number of photons (N = 10^6 and higher) [25]:

1. A photon is launched from air in the tissue geometry.
2. Reflection is calculated if crossing a boundary between two layers.
3. Refraction is calculated if moving in a layer with different refraction index (n).
4. A random pathlength is calculated, based on the μ_t of the tissue and the photon is moved.
5. The probability of absorption is calculated according to the μ_a of the tissue.
6. The random scattering angle is calculated based on the $p(cos\theta)$ of the tissue.
7. The photon continues propagating from step 2, until it is absorbed or detected.

Regarding absorption, there are two types of possible approaches:

- *Analog (discrete) absorption*: in this method, absorption is a single event and it terminates photon propagation. It mimics the real photons behavior more closely, but it is less efficient.
- *Continuous absorption*: in this method, instead of individual photons a "packet" of photons is launched at the same time. At every step a percentage of the packet is lost to absorption, according to Lambert-Beer law. It is computationally more efficient, but less accurate.

Since MC algorithms are computationally expensive, several optimizations are used to reduce the number of calculation necessary. One common example is the use of a cylindrical symmetry with pencil beam illumination, to reduce the problem from 3D to 2D. The output result of a MC simulation is normally the diffuse reflectance (R_d) of the tissue (either in the spatial domain or in the time domain, as shown in figure 3.1), however more complex models are available to calculate the fluence rate ϕ in a 3D mesh geometry [26, 27]

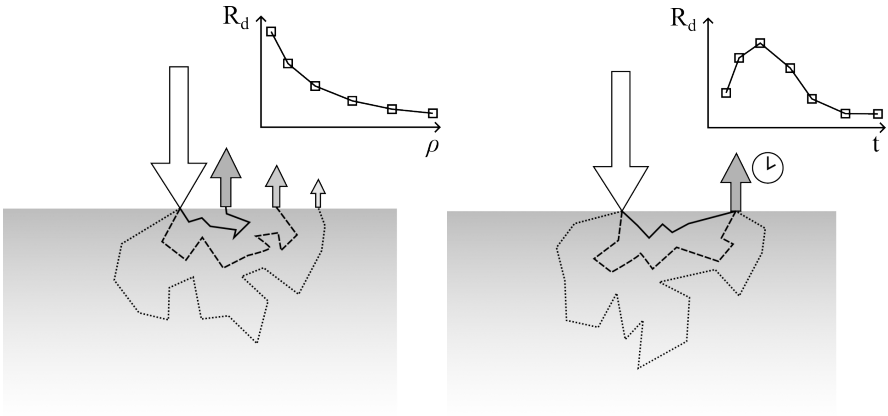

(a) (b)

Figure 3.1: Monte Carlo simulations of diffuse reflectance (R_d) in the space domain (a) and in the time domain (b).

White Monte Carlo: It's a particular Monte Carlo simulation that is used to efficiently emulate simulations with any arbitrary combinations of optical parameters (μ_a, μ_s') [28]. The base simulation has no absorption (hence the name "white") and unitary reduced scattering ($\mu_s' = 1mm^{-1}$). In order to match a simulation with a different absorption and scattering, first the μ_s' is altered by changing the particle density (as seen in equation 2.5). This can be done by simply expanding or contracting the coordinates and the pathlengths of the photons by multiplying them by the target $1/\mu_s'$. After having adjusted the density of the scattering particles, absorption is artificially introduced using Lambert-Beer law (equation 2.4), over each photon pathlength.
There are a few limitation over the usability of White MC, namely it can be only used on single-layer, semi-infinite homogeneous geometries. On the other hand it has the advantage of greatly reducing the simulation time, especially when hundreds or thousands of simulations are necessary, since only one White MC simulation is required and all the others can be derived by the application of a couple of equations.

Hankel Transform

In the previous section it was mentioned that Monte Carlo algorithms often make use of optimizations to reduce the simulation time, like using a geometry with a cylindrical symmetry in 2D. Another issue with Monte Carlo simulations is that it's not normally possible to directly perform simulations in the spatial frequency domain, so the data needs to be transformed from one domain to another.
The *Hankel Transform* (HT) is conceptually the equivalent of a 2D Fourier Transform in polar coordinates [29]. Given a function $f(r)$, the Hankel transform H(k_x) is defined

as:

$$\mathcal{H}(k_x) = \int_0^\infty f(r) J_0(r \cdot k_x)\, r\, dr \tag{3.10}$$

Where $J_0(r \cdot k_x)$ is the Bessel function of zeroth order of the first kind and $k_x = 2\pi f_x$. The HT can be used to transform MC simulations of $R_d(r)$ (spatial domain, in polar coordinates) to $R_d(f_x)$ (spatial frequency domain).

$$R_d(k_x) = \int_0^\infty R_d(r)\ J_0(r \cdot k_x)\, r\, dr \tag{3.11}$$

3.2 Data acquisition

The minimum instrumentation required to acquire SFDI data is shown in figure 3.2 and consists in a modulated light source (e.g. a digital projector), a sensor (e.g. a digital camera) and a processor to control the devices and store the data (e.g. a PC). Linear polarizing filters are often placed in front of the light source and the sensor, rotated by 90° with respect to each other to attenuate the specular reflection at the surface of the tissue. The components might range from anywhere low-cost to expensive research-grade instruments [30]. If a spectrometer is used as a sensor instead of an imaging device, another system operating in the spatial frequency domain is obtained, for a method called spatial frequency domain spectroscopy (SFDS) [31, 32]. SFDS is a technique similar to SFDI in which all the spatial information is lost in exchange for a much higher spectral resolution.
The acquisition process consists in projecting sinusoidal patterns at multiple f_x on the tissue, then capturing the diffuse reflectance from the tissue at each frequency. The reflectance intensity is constituted by the sum of an AC component and a DC component: $I = I_{AC} + I_{DC}$. Since only the modulated (AC) part is relevant to SFDI, a demodulation technique from signal processing must be employed. A very simple implementation is the three-phase demodulation method, adapted from the time domain to the spatial domain [16, 33]:

$$M_{AC}(f_i) = \frac{\sqrt{2}}{3}\sqrt{(I_1 - I_2)^2 + (I_2 - I_3)^2 + (I_3 - I_1)^2} \tag{3.12}$$

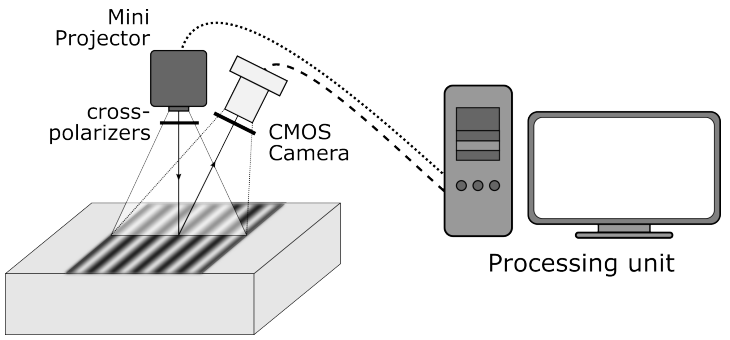

Figure 3.2: Schematic of a typical SFDI system

Where I_1, I_2, I_3 are the intensities of the images captured at three phases, with a phase shift of $\frac{2}{3}\pi$ each, and f_x is the spatial frequency. The modulated response $M_{AC}(f_x)$ is given by the product of the Source intensity I_0, the modulated transfer function (MTF) of the imaging system and the diffuse reflectance of the tissue R_d.

$$M_{AC} = I_0 \cdot MTF_{system} \cdot R_d \tag{3.13}$$

Since R_d is the quantity that is necessary to measure, it's possible to perform a calibration measurement on a reference phantom with known optical properties to compensate for the other terms:

$$R_d = \frac{M_{AC}}{M_{AC,ref}} \cdot R_{d,ref} \tag{3.14}$$

Where $M_{AC,ref}$ is the modulated response measured on the reference phantom and $R_{d,ref}$ is the predicted diffuse reflectance of the phantom, obtained from a direct model of light transport like SDA or Monte Carlo simulations.

3.3 Processing

Once the calibrated diffuse reflectance (R_d) of the tissue has been obtained from the measurement data, the next step is to determine what are its optical properties (μ_a, μ'_s). To do that, it's necessary to solve an inverse problem: until now only forward models of reflectance (like SDA and Monte Carlo) have been discussed, which take the optical properties (μ_a, μ'_s) in input to calculate R_d. The reverse is not an easy problem, as more than one combination of optical properties might exist that returns the same reflectance, so that R_d is often expressed as a function of a ratio of scattering and absorption: $R_d(\mu'_s/\mu_a)$ [34]. To solve this inverse problem, it's necessary to

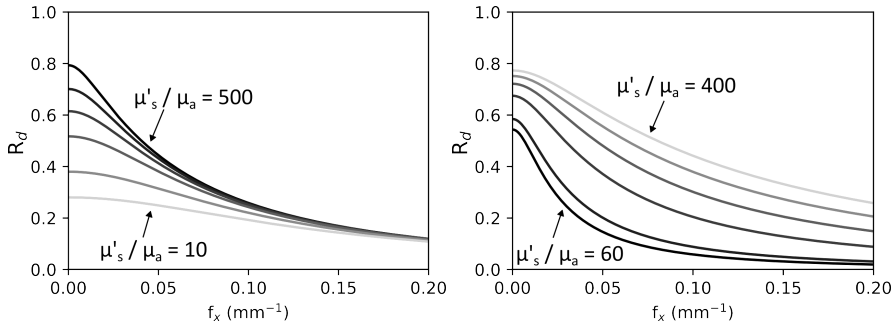

(a) (b)

Figure 3.3: How diffuse reflectance (R_d) changes in the spatial frequency domain. (a) When μ'_s is kept constant (1mm^{-1}), changes to μ_a generate contrast at low f_x. (b) When μ_a is kept constant (0.005mm^{-1}), changes in μ'_s generate contrast visible over all f_x.

add more dimensionality to the measurements, which for SFDI is done in the spatial frequency domain. As can be seen in figure 3.3, changes in μ_a and μ_s' generate contrast in R_d over f_x that is different for unique values of (μ_a, μ_s'). In particular, μ_a generates changes in R_d at low f_x and μ_s' generate changes over all f_x. Since in the SFD the inverse solution to $R_d(\mu_s'/\mu_a)$ is not uncertain anymore, it's possible to take measurements of R_d at (at least) 2 spatial frequencies and do a reverse fitting to the light transport model to obtain (μ_a, μ_s').
The process consists in an optimization problem, where an arbitrary initial guess of (μ_a, μ_s') is picked and used to model $R_{d,model}$. The modeled reflectance is then compared with the measured R_d and a minimization algorithm like least squares is used to iteratively update the values of (μ_a, μ_s') in search of a minimum of the difference between R_d and $R_{d,model}$. A more in-depth explanation and practical examples can be found in the OpenSFDI project [35].

3.4 Multi-frequency SFDI

Optical methods normally measure different volumes of tissue by exploiting the different penetration depth of light wavelengths [36, 37]. Techniques in the SFD have an ulterior advantage in this regard: the penetration depth of light patterns is also dependent on their spatial frequency f_x. Since the tissue acts as a low-pass filter on the patterns, higher frequencies have less penetration depth than lower frequencies. This property has been used with some success to try and reconstruct objects with optical contrast in depth [38, 39].
This section introduces an approach for processing SFDI data named *multi-frequency SFDI*. The method consists in subdividing the SFDI dataset in smaller subsets containing a few spatial frequencies each (see figure 3.4), which are then individually processed with the procedure described in section 3.3 to obtain (μ_a, μ_s'). The optical properties obtained from each subset have a different penetration depth in tissue, which depends on the average f_x of the subset.
In paper III [40] is shown how measurements on multi-layered targets processed with this method return different values of μ_s' depending on their f_x, while the same measurements on homogeneous targets lack this behaviour. This seems to indicate that the multi-frequency SFDI approach is effectively returning optical properties by sampling different depths at different f_x.

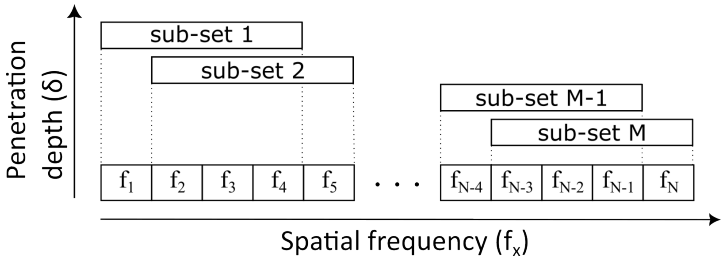

Figure 3.4: In multi-frequency SFDI, the dataset is divided in smaller subsets (that can be partially overlapping) and processed individually, so that the average f_x of each sub-set corresponds to a different penetration depth.

4

Optical phantoms

In order to calibrate optical devices and test the performance of new optical methods, a physical, traceable model of the target tissue is necessary. Biological tissues are highly variable between individuals and across time, so they are not a reliable source of consistent measurements. Optical phantoms are liquid or solid mixtures of dyes and scattering particles with controlled optical properties (μ_a, μ_s, g, n) and are widely used as a testing, validation and calibration tool in bio-optics applications [11, 41]. The advantages of using optical phantoms is to have standardized and stable reference with known optical properties that can be easily reproduced and exchanged between different research groups, to improve the consistency of measurements, identify the accuracy and limitations of optical methods and for devices calibration.
Another important use of optical phantoms is to make physical models of biological tissue, which might be otherwise not available or difficult to procure (see figure 4.1). This way it's possible to test devices and techniques on a consistent target, without the need to make use of animal models.

Optical phantoms are made up of three basic components: a *matrix*, a *scattering agent* and one (or more) *absorbers*.

Figure 4.1: A silicone skin phantom, with a pink dermis layer and a thin brown scattering layer mimicking skin melanoma.

Liquid phantoms

In liquid phantoms water-soluble absorbers and scattering agents are suspended in aqueous solution. The advantages of liquid phantoms are ease of fabrication and low cost, which makes them a suitable choice for producing them in large quantity. With liquid phantoms is also possible to perform measurements directly in the middle of the phantom, to avoid possible boundary effects. On the negative side they are less stable in time, more difficult to store and transport and can only be homogeneous. Also, the index of refraction (n) of water is different from skin.
For absorbing agents, any water-soluble ink or fluorescent molecule is suitable. For the scattering agent, polymer microspheres can be used, but the most common choices are organic lipid-based substances. Milk is a cheap alternative, but it's highly variable and not easy to reproduce. The most popular choice is a commercial lipid emulsion called *Intralipid* (or equivalent trademarked products), as it is much more stable and consistent between batches. Liquid phantoms are normally used to validate optical measurements of changes in haemoglobin oxygenation [43] and to test the detection limit and accuracy of devices over a large range of properties.

Gelatin phantoms

Gelatin phantoms are more stable than liquid-based ones and are particularly suited for embedding organic molecules and water-soluble inks. Gelatin allows to control the water content of the phantom, which can be used to alter its mechanical properties or increase the diffusion of molecules through the surface, to model drug diffusion dynamics. For scattering agent, Metal oxides such as TiO_2 or Al_2O_3 are a common choice. Other additive can be added to gelatin to improve its properties (e.g. formaldehyde, to increase its melting point) [44].
Gelatin phantoms are normally used to model water concentration in tissue [45] and to model molecular diffusion dynamics in drug delivery applications.

Silicone phantoms

The substrate in silicone phantoms is liquid silicone oil, that needs to be polymerized through vulcanization or (more commonly) with the addition of a curing agent. Silicone phantoms are more stable than liquid and gelatine phantoms and easier to store and transport. Their mechanical properties can be tuned and matched to the tissue elasticity. The index of refraction of silicone is also very close to real tissue. On the negative side, it's difficult to mix silicone oil with water-soluble molecules and the fabrication procedure is more complex. For the absorbing agents, inks can be used although water-soluble ones are more difficult to mix. For the scattering agents, inorganic microspheres and metal oxides (TiO_2 or Al_2O_3) are preferred, as they are more stable in time. The scattering coefficient of the phantom can be controlled by using particles with different sizes and concentration [11].
Silicone can be easily molded in any shape, so silicone phantoms are normally used to generate structures and layers with defined optical properties. Their high stability makes silicone phantoms also useful as calibration standards for optical systems.

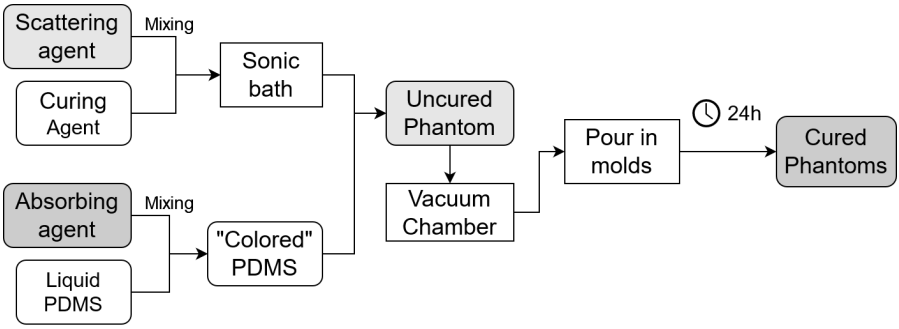

Figure 4.2: A chart of the process for fabricating silicone phantoms.

4.1 Fabrication process

The preparation of liquid and gelatin phantoms will not be discussed, as the process is quite straightforward. For silicone phantoms, the entire procedure is described in Saager et al. [41] and summarized in figure 4.2. The absorbing agents are mixed with the uncured silicone oil, while the scattering particles are mixed in the curing agent. To reduce clumps of particles that will change the scattering properties of the phantom, the curing agent is then placed into a sonic bath for 10-30 minutes. After that, the curing agent is mixed with the silicone oil and poured in molds of the desired shape and thickness. While the mixture is still liquid, the molds are placed in a vacuum chamber to remove any air bubbles that were formed while mixing, the presence of bubbles would otherwise change the scattering properties of the phantom. The phantoms are then left to cure on a level surface for at least 24 hours, until they become solid, and removed from the molds. Thin silicone phantoms can be overlapped to create multi-layers phantoms. When assembling the thin phantoms some air might remain between the layers, which would create a refractive index mismatch and alter the reflectance of the assembled phantom. To decrease this mismatch, ultrasound gel can be applied between the layers, then squeezed out as much as possible with a rolling pin.

5

Layered scattering model

Diffuse spectroscopy techniques (like SFDI) allow to indirectly measure biological molecules in a non-invasive way through the measurements of μ_a and μ_s' (as already discussed in chapter 2.2). Techniques like SFDI are already largely used in clinical applications, whether for the assessment of skin microcirculation [46], investigation of burn severity [47, 48, 49], Cancer detection [50, 51, 52] or skin optical characterization [53, 54].
A limitation of these techniques is that they operate on the assumption of a homogeneous target, whereas biological tissue is layered and full of heterogeneous structures. Chapter 2.1 describes the various layers that compose the skin and what are the principal cells and structures contained in them. Since skin (and biological tissue in general) is not homogeneous, the models used in optical methods should also contain layers with the appropriate optical properties.
Skin tissue is usually modeled as a combination of an epidermis with a fixed thickness d and a dermis with semi-infinite thickness, or large enough so that the penetration depth $\delta << d$ [22, 37, 55]. Most of these models are focused on light absorption and define the diffuse reflectance of the tissue depending on a difference in μ_a between the layers, or define the total μ_a as a linear combination of ($\mu_{a,top}$, $\mu_{a,bot}$) [37]. Scattering in the epidermis is assumed to be mostly irrelevant, so it is either ignored or set to be a fixed value [55]. Another disadvantage with these models is that a priori knowledge about the tissue is required, as they use a fixed thickness for the "epithelial" layer, with values of d estimated from literature on skin physiology [56, 57].

5.1 2-layer wound model

To overcome the limitations of previous models, a 2-layer model of light scattering that mimics the physiology of a healing wound was defined. The model's geometry consists of a thin scattering layer overlapped to a second thick scattering layer (see figure 5.1). In this model the features of interest are the difference in μ_s' between the layers, since it allows to differentiate between particles of different sizes (e.g. collagen fibres vs cells), and the thin layer thickness, which can be used as an objective parameter to evaluate the progression of epithelial growth in a wound. For this reason d is left as a free parameter, together with the scattering coefficients of the top and bottom layers ($\mu_{s,top}'$, $\mu_{s,bot}'$). The contribution from absorption becomes of secondary importance: haemoglobin absorption is mostly coming from deeper layers and, since

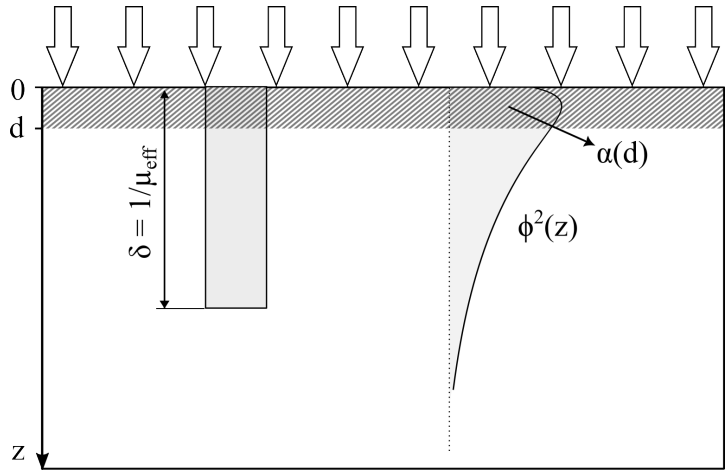

Figure 5.1: Geometry of the model. The top layer of thickness d has a scattering coefficient $\mu'_{s,top}$, and the bottom layer has a scattering coefficient $\mu'_{s,bot}$. On the left, is shown the linear partial volume contribution, given by d/δ. On the right is the fluence integral partial volume contribution $\alpha(d)$.

the epidermis is assumed to be damaged or missing, the absorption from melanin should also be negligible.

The 2-layer scattering model assumes the scattering we measure on a layered tissue is given by a linear combination of the μ'_s in the two layers:

$$\mu'_{s,mod} = \alpha(d)\ \mu'_{s,top} + (1 - \alpha(d))\ \mu'_{s,bot} \tag{5.1}$$

where $\alpha(d)$ is the partial volume contribution of scattering from the top layer, so it has a dependence on d. Typical partial volume models assume a linear contribution expressed as a ratio between d and the penetration depth of light $\delta = 1/\mu_{eff}$ [37]. This representation is a very simple approximation, which doesn't take in consideration the real distribution of photons inside the tissue. Since light intensity decays exponentially with depth, this tends to overestimate the contribution from the bottom layer. In this chapter a partial volume contribution $\alpha(d)$ is presented, obtained by integrating a function that describes the density of photons in depth. For this purpose, the *photon hitting density* (PHD) [58] was chosen, which is a measure of how much time a photon spends in a determined volume while moving from the source to the detector. In a SFDI system, both the source (planar illumination) and the detector (wide-field imaging) have the same probability distribution function of how deep a photon can reach, which is represented by the light fluence rate (ϕ). Multiplying the source and detector functions gives a PHD equal to the fluence squared (ϕ^2). The

partial volume contribution $\alpha(d)$ then becomes:

$$\alpha(d) = \frac{\int_0^d \phi^2(z)\, dz}{\int_0^\infty \phi^2(z)\, dz} \tag{5.2}$$

In chapter 3.1 multiple models of light fluence have been defined, which can be used in equation 5.2, and their individual performances have been tested on layered optical phantoms, as described in paper IV [23].

For the purpose of this thesis work, ϕ is approximated with a homogeneous fluence model calculated using the experimental SFDI measurements of (μ_a, μ_s'), which are assumed to be homogeneous. Note that fluence is also dependent on f_x, so when operating in the spatial frequency domain, equation 5.2 becomes:

$$\alpha(d, f_x) = \frac{\int_0^d \phi^2(z, f_x)\, dz}{\int_0^\infty \phi^2(z, f_x)\, dz} \tag{5.3}$$

5.2 Inverse problem

The scattering model defined in equation 5.1 has three free parameters (d, $\mu_{s,top}$, $\mu_{s,bot}'$). In the direct model, if these parameters are known, it's possible to calculate an estimate of the measured μ_s' on a 2-layered target, as shown in paper IV on layered silicone phantoms [23]. This is however not enough for practical applications. The model parameters are more interesting from a clinical standpoint, as $\mu_{s,top}'$, $\mu_{s,bot}'$ can be used to estimate the microstructure of the two layers and d is an objective metric to evaluate the re-epithelization of a wound.

To obtain the model parameters, we need to solve a minimization problem:

$$\min\{\mu_{s,meas}' - \mu_{s,mod}'(d, \mu_{s,top}', \mu_{s,bot}')\} \tag{5.4}$$

Where $\mu_{s,meas}'$ is the scattering coefficient measured with SFDI and $\mu_{s,mod}'$ is the model of the measurements. Since there are three unknowns, at least three different measurements are necessary for the problem to be determined. Multiple measurements can be introduced in the SFD using the multi-frequency SFDI approach described in chapter 3.4. The problem then becomes:

$$\min \begin{cases} \mu_{s,meas}'(f_{x1}) - \mu_{s,mod}'(f_{x1}, d, \mu_{s,top}', \mu_{s,bot}') \\ \mu_{s,meas}'(f_{x2}) - \mu_{s,mod}'(f_{x2}, d, \mu_{s,top}', \mu_{s,bot}') \\ \mu_{s,meas}'(f_{x3}) - \mu_{s,mod}'(f_{x3}, d, \mu_{s,top}', \mu_{s,bot}') \\ \qquad\qquad ... \end{cases} \tag{5.5}$$

Where $\mu_{s,meas}'(f_{x\,i})$ are the measured scattering coefficients in each sub-set from the multi-frequency SFDI. Note that f_x is also present in the model, as the partial volume

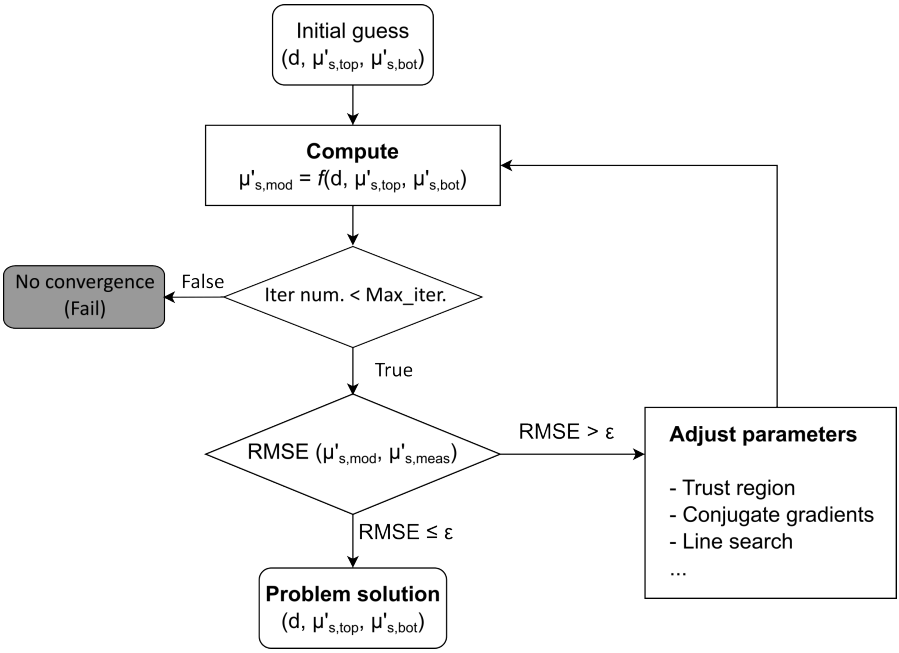

Figure 5.2: Flowchart of the inverse solving algorithm

contributions $\alpha(d, f_x)$ depend on ϕ, which is also f_x-dependent. The more measurements in the SFD are introduced, the more the solution will be accurate.

Paper V [59] Describes an iterative algorithm to solve the minimization problem in equation 5.5. The flow of the algorithm can be seen in figure 5.2. An arbitrary initial guess is chosen for the parameters (d, $\mu_{s,top}$, $\mu'_{s,bot}$) and the root mean square error (RMSE) is calculated from the difference between $\mu'_{s,meas}$ and $\mu'_{s,mod}$. The RMSE is used as a cost function to minimize by iteratively adjusting the parameters (d, $\mu_{s,top}$, $\mu'_{s,bot}$), to find their combination that gives the μ'_s model as close as possible to the data. The iteration is repeated as long as the cost function is greater than an arbitrary small tolerance value ε or a maximum number of iterations is reached, meaning that the algorithm is not converging because it's stuck in a non-optimal local minimum. To reduce non-convergence due to a bad choice of initial parameters guess, the minimization is repeated with 1000 random initial guesses in the parameters space and the converged solution with the lowest RMSE is chosen as the final result.
There are several gradient-based optimization algorithms that can be used, but it's outside the scope of this thesis to discuss what algorithm is the most appropriate one to the problem.

Coupling of parameters

Separating the effects of optical properties have on reflectance is not an easy problem, because of the principle of similarity. In chapter 2.2 was already shown that

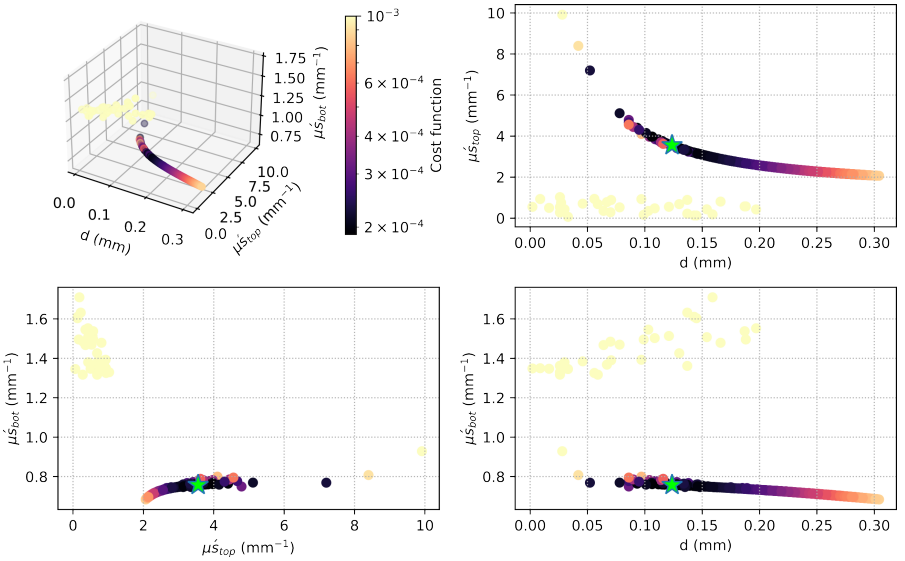

Figure 5.3: Example of converged solutions of 1000 random initial guesses in the 3D parameter space, after minimization. The green star is the solution with the smallest RMSE. The SFDI data was measured at 536nm on a 2-layered phantom with top layer thickness of 0.13mm.

different combinations of g and μ_s can have the same overall effect on light scattering (expressed by μ_s'), even if caused by different physical phenomena. The similarity effect is extended to the diffuse reflectance R_d, as it can be expressed as a function of the ratio of reduced scattering and absorption: $R_d(\mu_s'/\mu_a)$ [34]. This means that an infinite number of pairs (μ_a, μ_s') exist, that give the same R_d value and it's necessary to introduce additional dimensionality in our measurements (e.g. in the SFD) to be able to differentiate them, as already discussed in chapter 3.3.

When dealing with multi-layer models, the thickness of the layers introduces a new level of uncertainty and the optical parameters are often combined into a single one called *optical thickness* or *optical depth* ($\tau = d(\mu_a + \mu_s')$), as shown in a work by Yudowsky et al. [55].

In the 2-layer models of scattering defined in equation 5.1 there is strong correlation between the thickness of the top layer and $\mu_{s,top}'$, as it is not possible to determine whether a change in R_d is due to a change in $\mu_{s,top}'$ or d. This correlation is shown in paper V, in the converged inverse solution. Figure 5.3 shows an example of the 1000 random initial guesses in the parameter space after convergence. The data in the figure comes from the study done in paper V, done on 2-layer silicone scattering phantoms, with a top layer thickness of 0.13mm. It is possible to see that the initial random samples (except for a few non-converging points) converge to a curve in the 3D parameter space, rather than a single global minimum, indicating that any solution along this curve will give very similar results. The correlation seems to be especially between d and $\mu_{s,top}'$, which exhibit an inverse proportionality as anticipated.

This coupling of d and $\mu'_{s,top}$ is however not absolute. There seems to be a global minimum along the curve (marked by the green star), which is quite close to the actual solution ($d = 0.13mm$, $\mu'_{s,top} = 2.93mm^{-1}$, $\mu'_{s,bot} = 0.83mm^{-1}$). This might be an indication that introducing depth sensitivity to the measurements through multi-frequency SFDI is helping to solve the uncertainty brought by the principle of similarity.

6

Discussion

The objective of this thesis was to improve the SFDI technique with the aim of obtaining more information from light scattering, that could be useful in the study of skin conditions and diagnosis of wound healing. To pursue these objectives, we have:

- Built and characterized a hand-held SFDI system, that has been successfully used in multiple projects in collaboration with clinical partners.
- Developed and tested the multi-frequency SFDI approach to data processing, that introduces depth information.
- Developed a 2-layer scattering model with partial volume contributions based on light fluence, which mimics the scattering difference due to microscopic changes in the wound structure. The model accuracy has been validated on layered silicone phantoms.
- Developed an inverse solver algorithm to extract optical parameters of interest from the multi-frequency SFDI data using the 2-layer scattering model. The algorithm has been tested on silicone phantoms and ex-vivo burn wounds.

6.1 Future work

The 2-layer model we developed in paper IV is still based on an homogeneous approximation of the fluence, so it's not able to model the data accurately in the entire range of parameters. A more realistic discontinuous model of ϕ should be able to improve the accuracy of the integral partial volume contribution α. In order to define a 2-layer model of fluence, previous knowledge of optical parameters in the two layers is necessary, which makes it an interesting problem as they are the unknowns we aim to estimate. A possible approach is to use the homogeneous model of ϕ to make an initial estimate of $(\mu_a,\ \mu_s')$ in the two layer, then use these layer-specific optical properties to iteratively refine the estimate by using a 2-layer ϕ model.

This thesis was focused on analytical models of ϕ, mainly because of the faster computing times. Monte Carlo simulations models of fluence are possible (albeit extremely time consuming) and could return more accurate results, especially in the regimes where the diffusion approximations are not valid. A compromise between analytical solutions and pure simulations of ϕ could be hybrid or semi-empirical 2-layer models like the one from Horan et al. [60].

Lastly, the range of thickness in the skin layers and healing epithelium that are the subject of the study (10 - 100μm) are smaller than the ones were investigated in this work (0.1 - 1mm). By increasing the range of measured spatial frequencies ($f_x > 0.5$ mm^{-1}), it's possible to sample even more superficial volumes of tissue, which can help in discriminating scattering contrast in smaller layers. The problem, however, is that for very small distances the SDA assumptions are not valid anymore and we enter the *sub-diffuse* scattering regime [15, 61]. Applications using high-order scattering parameters already exist, both in the for SFDI [62] and single fibre spectroscopy [63] and should be relatively easy to implement in our models.

7

Summary of papers

7.1 Paper I

Handheld multispectral imager for quantitative skin assessment in low-resource settings

In this article we describe the way to build an SFDI device prototype using low-cost commercial components. We have compared the measurements made with this low-cost device with another research-grade instrument to show that the data obtained from the former instrument is accurate enough to be used in practical applications. The commercial components used in the prototype are based on broadband RGB LEDs and colored filters, which is a limiting factor on the spectral information that can be obtained from these devices. To overcome this limitation, we introduced the concept of *cross-channels*, which are additional colored bands found on the spectral overlap of the LED light sources and the sensor color filters. The introduction of cross-channels adds a few additional spectral bands at no cost in devices that are normally limited to three colors, improving the capability of the device to detect biological species from their absorption and scattering spectral signatures.

7.2 Paper II

miR-155 mediates multiple gene regulations pertinent to the role of human adipose-derived mesenchymal stem cells in skin repair

In this collaboration article, a porcine animal model was used to study the efficacy of several wound regeneration therapies based on stem cells. Multiple surgical wounds were provoked under general anesthesia on two pigs included in the study. The wounds were then injected with different compositions of stem cells and negative controls in a double blind setup. The condition of the wounds has been assessed right after the treatment and at other two time points every 7 days. After the two weeks have passed, the animals were sacrificed and biopsies were performed on the wounds, to perform more specific measurements like histological analysis and protein analysis. We contributed to the study by performing SFDI measurements on the

wounds at each time point and analysing the absorption and scattering data using the multi-frequency SFDI approach mentioned in paper III. Our measurements showed a significant difference between the stem cells treated wounds and the negative controls, offering an additional validation of the efficacy of the therapies in exam.

7.3 Paper III

Beneath the skin: multi-frequency SFDI to detect thin layers of skin using light scattering

Stem cells based therapies are a promising approach in the field of regenerative medicine, but the current methods used for the evaluation of these treatments are either destructive (requiring biopsies) or not specific enough (visual inspection). The problem we aim to solve in this conference proceedings is how to evaluate the progression of wound healing in a way that is both objective, non-invasive and capable of measuring its evolution in time. The solution we propose is to use SFDI to measure the scattering coefficient μ_s', which contains information about the microscopical structures in the tissue and can be used as a biomarker for the changes happening during the proliferation and remodeling phases of wound healing. Measuring the μ_s' coefficient is not enough to properly interpret these physiological changes, due to the multi-layered nature of biological tissue. For this reason we introduce the concept of *multi-frequency SFDI*, which allows us to change the penetration depth of light patterns and obtain depth-resolved SFDI data. We also developed a 2-layer scattering model that mimics a healing wound and present some initial results obtained by comparing the multi-frequency SFDI data to the model.

7.4 Paper IV

Multi-frequency SFDI: a depth-resolved optical scattering model to isolate scattering contrast in thin layers of skin

In this article we expand the preliminary work introduced in Paper III. Light scattering is an underutilized source of information for biological phenomena. When operating in a biological setting however, measuring scattering (μ_s') using common optical methods is subject to limitations due to the fact that these methods are based on light diffusion models. These models work on the assumption that light propagates through a thick and homogeneous volume of tissue, which is not the case in biological tissue. In order to overcome this limitation, we developed a 2-layer scattering model where the partial volumes contribution of each layer are derived from light fluence. We employed three different analytical derivations of light fluence, one of which was derived by ourselves. By using multi-frequency SFDI it is possible to obtain depth-resolved scattering measurements, which change according to the thickness of the thin layer and the ratio of the two μ_s'. Data obtained from the 2-layer model was compared with measurements made on silicone scattering phantoms of

known properties, showing that the multi-frequency measurements can be expressed as a combination of the μ_s' in each layer.

7.5 Paper V

Multi-frequency SFDI: inverse solving algorithm to reconstruct depth-resolved scattering properties in wound healing

After having shown that the μ_s' measured on 2-layered phantoms can be modeled as a combination of the μ_s' in the two layers in paper IV, we have developed an iterative inverse-solving algorithm that takes in input the multi-frequency SFDI measurements and fits them to our 2-layer model, in order to obtain the free model parameters $\mu'_{s_{top}}$, $\mu'_{s_{bot}}$ and d. The performance of the algorithm was studied on thin silicone phantoms over a range of thicknesses, to determine within which limits we can expect results that are reliable enough to be of practical use. The aim of the article is to obtain parameters that can be used to help with the assessment of healing wounds. The scattering coefficients can be correlated to the formation of microscopical structures (e.g. collagen and cell nuclei), which can help in establishing if new epithelial cells are being formed, or if there are irregularities in the extracellular matrix (ECM). The thickness of the thin epithelial layer (d) is also an objective parameter useful in evaluating the efficacy of different treatments and it's a type of information that is usually only available through invasive methods (i.e biopsy). As a sample case, multi-frequency SFDI measurements were taken on ex-vivo burn wounds treated with stem-cells based therapies, and the model parameters were calculated with the inverse-solving algorithm. The results have been then interpreted and compared with the ones obtained from cell histology.

Bibliography

[1] Almadani YH, Vorstenbosch J, Davison PG, and Murphy AM. "Wound Healing: A Comprehensive Review". In: *Semin Plast Surg*. 35.3 (2021). DOI: 10.1055/s-0041-1731791.

[2] Akriti Gupta and Pramod Kumar. "Assessment of the histological state of the healing wound". In: *Plastic and Aesthetic Research* 2.5 (2015), p. 239. ISSN: 2347-9264. DOI: 10.4103/2347-9264.158862. URL: https://www.researchgate.net/publication/281844759_Assessment_of_the_histological_state_of_the_healing_wound.

[3] Daniela S. Masson-Meyers, Thiago A.M. Andrade, Guilherme F. Caetano, Francielle R. Guimaraes, Marcel N. Leite, Saulo N. Leite, and Marco Andrey C. Frade. "Experimental models and methods for cutaneous wound healing assessment". In: *International Journal of Experimental Pathology* 101.1-2 (Feb. 2020), pp. 21–37. DOI: 10.1111/IEP.12346.

[4] T Velnar, T Bailey, and V Smrkolj. "The Wound Healing Process: An Overview of the Cellular and Molecular Mechanisms". In: *Journal of International Medical Research* 37.5 (2009), pp. 1528–1542. DOI: 10.1177/147323000903700531. URL: https://doi.org/10.1177/147323000903700531.

[5] J. Gordon Betts, Kelly A. Young, James A. Wise, Eddie Johnson, Brandon Poe, Dean H. Kruse, Oksana Korol, Jody E. Johnson, Mark Womble, and Peter DeSaix. *Anatomy and Physiology 2e*. OpenStax, 2022. URL: https://openstax.org/books/anatomy-and-physiology-2e/pages/1-introduction.

[6] Maranke I. Koster. "Making an epidermis". In: *Annals of the New York Academy of Sciences* 1170 (2009), pp. 7–10. DOI: 10.1111/j.1749-6632.2009.04363.x.

[7] Muhammad Irfan-Maqsood. "Classification of Wounds: Know before Research and Clinical Practice". In: *Cell Therapy and Regenerative Medicine Journal* 1 (Mar. 2016), p. 79. DOI: 10.15562/ctrm.21.

[8] Valery Tuchin. "Tissue Optics and Photonics: Light-Tissue Interaction". In: *Journal of Biomedical Photonics Engineering* 1 (June 2015), pp. 98–134. DOI: 10.18287/JBPE-2015-1-2-98.

[9] Irving Bigio and Sergio Fantini. *Quantitative Biomedical Optics: Theory, Methods, and Applications*. Jan. 2016. ISBN: 9780521876568. DOI: 10.1017/CBO9781139029797.

[10] Hsin-i Wu Lihong V. Wang. *Biomedical Optics: Principles and Imaging*. Wiley, 2012. ISBN: 978-0-470-17700-6.

[11] Rolf B. Saager, Alan Quach, Rebecca A. Rowland, Melissa L. Baldado, and Anthony J. Durkin. "Low-cost tissue simulating phantoms with adjustable wavelength-dependent scattering properties in the visible and infrared ranges". In: *Journal of Biomedical Optics* 21.6 (2016), p. 067001. ISSN: 1083-3668. DOI: 10.1117/1.jbo.21.6.067001.

[12] Judith R. Mourant, James P. Freyer, Andreas H. Hielscher, Angelia A. Eick, Dan Shen, and Tamara M. Johnson. "Mechanisms of light scattering from biological cells relevant to noninvasive optical-tissue diagnostics". In: *Applied Optics* 37.16 (1998), p. 3586. ISSN: 0003-6935. DOI: 10.1364/ao.37.003586.

[13] W.F. Cheong, S.A. Prahl, and A.J. Welch. "A review of the optical properties of biological tissues". In: *IEEE Journal of Quantum Electronics* 26.12 (1990), pp. 2166–2185. DOI: 10.1109/3.64354.

[14] Nick Pfeiffer and Glenn H. Chapman. "Successive order, multiple scattering of two-term Henyey-Greenstein phase functions". In: *Optics Express* 16.18 (Sept. 2008), p. 13637. ISSN: 1094-4087. DOI: 10.1364/oe.16.013637. URL: https://www.osapublishing.org/oe/abstract.cfm?uri=oe-16-18-13637.

[15] David M McClatchy, Elizabeth J Rizzo, Wendy A Wells, Philip P Cheney, Jeeseong C Hwang, Keith D Paulsen, Brian W Pogue, and Stephen C Kanick. "Wide-field quantitative imaging of tissue microstructure using sub-diffuse spatial frequency domain imaging - supplementary". In: *Optica* 3.6 (2016), p. 613. DOI: 10.1364/optica.3.000613.

[16] David J. Cuccia, Frederic Bevilacqua, Anthony J. Durkin, Frederick R. Ayers, and Bruce J. Tromberg. "Quantitation and mapping of tissue optical properties using modulated imaging". In: *Journal of Biomedical Optics* 14.2 (2009), p. 024012. ISSN: 10833668. DOI: 10.1117/1.3088140. URL: https://www.ncbi.nlm.nih.gov/pubmed/19405742.

[17] Hsin-i Wu Lihong V. Wang. *Biomedical Optics: Principles and Imaging*. Wiley, 2012. ISBN: 978-0-470-17700-6.

[18] Tsong-Tseh Tsay, Lars O. Svaasand, Bruce J. Tromberg, Richard C. Haskell, Matthew S. McAdams, and Ti-Chen Feng. "Boundary conditions for the diffusion equation in radiative transfer". In: *Journal of the Optical Society of America A* 11.10 (Oct. 1994), pp. 2727–2741. ISSN: 1520-8532. DOI: 10.1364/JOSAA.11.002727.

[19] J. Joseph, Warren Wiscombe, and J. Weinman. "The Delta-Eddington Approximation for Radiative Flux Transfer". In: *Journal of the Atmospheric Sciences* 33 (Jan. 1977). DOI: 10.1175/1520-0469(1976)033<2452:TDEAFR>2.0.CO;2.

[20] Stefan A. Carp, Scott A. Prahl, and Vasan Venugopalan. "Radiative transport in the delta-P1 approximation: accuracy of fluence rate and optical penetration depth predictions in turbid semi-infinite media". In: *Journal of Biomedical Optics* 9.3 (May 2004), pp. 632–647. ISSN: 1083-3668. DOI: 10.1117/1.1695412.

[21] L. G. Henyey and J. L. Greenstein. "Diffuse radiation in the Galaxy." In: *Astrophysical Journal* 93 (Jan. 1941), pp. 70–83. DOI: 10.1086/144246.

[22] In Seok Seo. “Diffuse Reflectance Spectroscopy for Epithelial Tissues”. PhD thesis. University of California, Irvine, 2007. Chap. Appendix A, p. 680.

[23] Luigi Belcastro, Hanna Jonasson, and Rolf B. Saager. “Multi-frequency SFDI: a depth-resolved optical scattering model to isolate optical properties in thin layers of skin”. In: *JBO Manuscript* (2023).

[24] Frederik Michel Dekking, Cornelis Kraaikamp, Hendrik Paul Lopuhaä, and Ludolf Erwin Master. *A Modern Introduction to Probability and Statistics*. Springer London, 2005. ISBN: 978-1-84628-168-6.

[25] Lihong Wang, Steven L. Jacques, and Liqiong Zheng. “MCML—Monte Carlo modeling of light transport in multi-layered tissues”. In: *Computer Methods and Programs in Biomedicine* 47.2 (July 1995), pp. 131–146. ISSN: 0169-2607. DOI: 10.1016/0169-2607(95)01640-F.

[26] Günther H. Hartmann and Pedro Andreo. “Fluence calculation methods in Monte Carlo dosimetry simulations”. In: *Zeitschrift für Medizinische Physik* 29.3 (Aug. 2019), pp. 239–248. ISSN: 0939-3889. DOI: 10.1016/J.ZEMEDI.2018.08.003.

[27] Julia L. Sandell and Timothy Zhu. “Monte Carlo simulation of light fluence calculation during pleural PDT”. In: *Proceedings of SPIE–the International Society for Optical Engineering* 8568 (Feb. 2013), 85680U. ISSN: 16057422. DOI: 10.1117/12.2005944. URL: https://www.ncbi.nlm.nih.gov/pmc/articles/PMC4437723/.

[28] Alwin Kienle and Michael S Patterson. “Determination of the optical properties of turbid media from a single Monte Carlo simulation”. In: *Physics in Medicine Biology* 41.10 (Oct. 1996), p. 2221. DOI: 10.1088/0031-9155/41/10/026. URL: https://dx.doi.org/10.1088/0031-9155/41/10/026.

[29] Urs Graf. “Hankel Transforms”. In: *Introduction to Hyperfunctions and Their Integral Transforms: An Applied and Computational Approach*. Birkhäuser Basel, 2010, pp. 337–372. ISBN: 978-3-0346-0408-6. DOI: 10.1007/978-3-0346-0408-6_7. URL: https://doi.org/10.1007/978-3-0346-0408-6_7.

[30] Luigi Belcastro, Hanna Jonasson, Tomas Strömberg, and Rolf B. Saager. “Handheld multispectral imager for quantitative skin assessment in low-resource settings”. In: *Journal of Biomedical Optics* 25.08 (Aug. 2020), p. 1. ISSN: 1560-2281. DOI: 10.1117/1.jbo.25.8.082702. URL: https://www.spiedigitallibrary.org/terms-of-use.

[31] Rolf B. Saager, An N. Dang, Samantha S. Huang, Kristen M. Kelly, and Anthony J. Durkin. “Portable (handheld) clinical device for quantitative spectroscopy of skin, utilizing spatial frequency domain reflectance techniques”. In: *Review of Scientific Instruments* 88.9 (2017), p. 94302. ISSN: 10897623. DOI: 10.1063/1.5001075. URL: https://www.ncbi.nlm.nih.gov/pubmed/28964218.

[32] Rolf B. Saager, Melissa L. Baldado, Rebecca A. Rowland, Kristen M. Kelly, and Anthony J. Durkin. "Method using in vivo quantitative spectroscopy to guide design and optimization of low-cost, compact clinical imaging devices: emulation and evaluation of multispectral imaging systems". In: *Journal of Biomedical Optics* 23.04 (Apr. 2018), p. 1. ISSN: 1083-3668. DOI: 10.1117/1.JBO.23.4.046002.

[33] M. A. A. Neil, R. Juškaitis, and T. Wilson. "Method of obtaining optical sectioning by using structured light in a conventional microscope". In: *Optics letters* 22.24 (Dec. 1997), p. 1905. ISSN: 0146-9592. DOI: 10.1364/OL.22.001905. URL: https://pubmed.ncbi.nlm.nih.gov/18188403/.

[34] George Zonios and Aikaterini Dimou. "Modeling diffuse reflectance from semi-infinite turbid media: application to the study of skin optical properties". In: *Opt. Express* 14.19 (Sept. 2006), pp. 8661–8674. DOI: 10.1364/OE.14.008661. URL: https://opg.optica.org/oe/abstract.cfm?URI=oe-14-19-8661.

[35] Matthew B. Applegate, Kavon Karrobi, Joseph P. Angelo Jr., Wyatt M. Austin, Syeda M. Tabassum, Enagnon Aguénounon, Karissa Tilbury, Rolf B. Saager, Sylvain Gioux, and Darren M. Roblyer. "OpenSFDI: an open-source guide for constructing a spatial frequency domain imaging system". In: *Journal of Biomedical Optics* 25.1 (2020), p. 016002. DOI: 10.1117/1.JBO.25.1.016002. URL: https://doi.org/10.1117/1.JBO.25.1.016002.

[36] Rolf B. Saager, Mihaela Balu, Viera Crosignani, Ata Sharif, Anthony J. Durkin, Kristen M. Kelly, and Bruce J. Tromberg. "In vivo measurements of cutaneous melanin across spatial scales: using multiphoton microscopy and spatial frequency domain spectroscopy". In: *Journal of Biomedical Optics* 20.6 (June 2015), p. 066005. ISSN: 1083-3668. DOI: 10.1117/1.jbo.20.6.066005. URL: http://biomedicaloptics.spiedigitallibrary.org/article.aspx?doi=10.1117/1.JBO.20.6.066005.

[37] Rolf B. Saager, Alex Truong, Anthony J. Durkin, and David J. Cuccia. "Method for depth-resolved quantitation of optical properties in layered media using spatially modulated quantitative spectroscopy". In: *Journal of Biomedical Optics* 16.7 (July 2011), p. 077002. ISSN: 1083-3668. DOI: 10.1117/1.3597621.

[38] David J Cuccia, Frederic Bevilacqua, Anthony J Durkin, and Bruce J Tromberg. "Modulated imaging: quantitative analysis and tomography of turbid media in the spatial-frequency domain". In: *Optics Letters* 30.11 (2008), p. 1354. ISSN: 0146-9592. DOI: 10.1364/ol.30.001354. URL: https://www.ncbi.nlm.nih.gov/pubmed/15981531.

[39] Soren D. Konecky, Amaan Mazhar, David Cuccia, Anthony J. Durkin, John C. Schotland, and Bruce J. Tromberg. "Quantitative optical tomography of subsurface heterogeneities using spatially modulated structured light". In: *Optics Express* 17.17 (Aug. 2009), p. 14780. ISSN: 1094-4087. DOI: 10.1364/oe.17.014780.

[40] Luigi Belcastro, Hanna Jonasson, Tomas Strömberg, Ahmed Elserafy, Rolf Saager Luigi Belcastro, and Rolf B Saager. "Beneath the skin: multi-frequency SFDI to detect thin layers of skin using light scattering". In: *https://doi.org/10.1117/12.2648545* 12352 (Mar. 2023), pp. 44–48. ISSN: 16057422. DOI: 10.1117/12.2648545.

[41] Rolf B. Saager, Clement Kondru, Kendrew Au, Kelly Sry, Frederick Ayers, and Anthony J. Durkin. "Multilayer silicone phantoms for the evaluation of quantitative optical techniques in skin imaging". In: *Design and Performance Validation of Phantoms Used in Conjunction with Optical Measurement of Tissue II* 7567 (2010), p. 756706. DOI: 10.1117/12.842249.

[42] Deep Thought. "The answer to life, the universe, and everything". In: *The Hitchhiker's Guide to the Galaxy* (1979).

[43] Motasam Majedy, Rolf B. Saager, Tomas Strömberg, and Marcus Larsson. "Spectral characterization of liquid hemoglobin phantoms with varying oxygenation states". In: *Journal of Biomedical Optics* 27.7 (2022). ISSN: 1083-3668.

[44] Brian W. Pogue and Michael S. Patterson. "Review of tissue simulating phantoms for optical spectroscopy, imaging and dosimetry". In: *Journal of Biomedical Optics* 11.4 (2006), p. 041102. ISSN: 10833668. DOI: 10.1117/1.2335429.

[45] Hanna Jonasson, Chris D. Anderson, and Rolf B. Saager. "Water and hemoglobin modulated gelatin-based phantoms to spectrally mimic inflamed tissue in the validation of biomedical techniques and the modeling of microdialysis data". In: *Journal of Biomedical Optics* 27.7 (2022), p. 074712. DOI: 10.1117/1.JBO.27.7.074712. URL: https://doi.org/10.1117/1.JBO.27.7.074712.

[46] Amr Yafi, Thomas S Vetter, Thomas Scholz, Sarin Patel, Rolf B Saager, David J Cuccia, Gregory R Evans, and Anthony J Durkin. "Postoperative quantitative assessment of reconstructive tissue status in a cutaneous flap model using spatial frequency domain imaging." In: *Plastic and reconstructive surgery* 127.1 (Jan. 2011), pp. 117–30. ISSN: 1529-4242. DOI: 10.1097/PRS.0b013e3181f959cc.

[47] John Quan Nguyen, Christian Crouzet, Tuan Mai, Kathleen Riola, Daniel Uchitel, Lih-Huei Liaw, Nicole Bernal, Adrien Ponticorvo, Bernard Choi, and Anthony J. Durkin. "Spatial frequency domain imaging of burn wounds in a preclinical model of graded burn severity". In: *Journal of Biomedical Optics* 18.6 (June 2013), p. 066010. ISSN: 1083-3668. DOI: 10.1117/1.jbo.18.6.066010.

[48] Amaan Mazhar, Steve Saggese, Alonda C. Pollins, Nancy L. Cardwell, Lillian B. Nanney, and David J. Cuccia. "Noncontact imaging of burn depth and extent in a porcine model using spatial frequency domain imaging". In: *Journal of Biomedical Optics* 19.8 (Aug. 2014), p. 086019. ISSN: 1083-3668. DOI: 10.1117/1.JBO.19.8.086019.

[49] Adrien Ponticorvo, Rebecca Rowland, Melissa Baldado, Gordon T. Kennedy, Anna Marie Hosking, David M. Burmeister, Robert J. Christy, Nicole P. Bernal, and Anthony J. Durkin. "Spatial Frequency Domain Imaging (SFDI) of clinical burns: A case report". In: *Burns Open* 4.2 (Apr. 2020), pp. 67–71. ISSN: 24689122. DOI: 10.1016/j.burnso.2020.02.004.

[50] Daniel J. Rohrbach, Daniel Muffoletto, Jonathan Huihui, Rolf Saager, Kenneth Keymel, Anne Paquette, Janet Morgan, Nathalie Zeitouni, and Ulas Sunar. "Preoperative Mapping of Nonmelanoma Skin Cancer Using Spatial Frequency Domain and Ultrasound Imaging". In: *Academic Radiology* 21.2 (Feb. 2014), pp. 263–270. ISSN: 1076-6332. DOI: 10.1016/J.ACRA.2013.11.013.

[51] "Characterization of nonmelanoma skin cancer for light therapy using spatial frequency domain imaging". In: *Biomedical Optics Express* 6.5 (May 2015), pp. 1761–1766. ISSN: 2156-7085. DOI: 10.1364/BOE.6.001761.

[52] R. B. Saager, D. J. Cuccia, S. Saggese, K. M. Kelly, and A. J. Durkin. "A Light Emitting Diode (LED) based spatial frequency domain imaging system for optimization of photodynamic therapy of nonmelanoma skin cancer: Quantitative reflectance imaging". In: *Lasers in Surgery and Medicine* 45.4 (2013), pp. 207–215. ISSN: 01968092. DOI: 10.1002/lsm.22139.

[53] Amaan Mazhar, Seyed A. Sharif, J. David Cuccia, J. Stuart Nelson, Kristen M. Kelly, and Anthony J. Durkin. "Spatial frequency domain imaging of port wine stain biochemical composition in response to laser therapy: A pilot study". In: *Lasers in Surgery and Medicine* 44.8 (Oct. 2012), pp. 611–621. ISSN: 01968092. DOI: 10.1002/lsm.22067.

[54] Frederick R. Ayers, David J. Cuccia, Kristen M. Kelly, and Anthony J. Durkin. "Wide-field spatial mapping of in vivo tattoo skin optical properties using modulated imaging". In: *Lasers in Surgery and Medicine* 41.6 (Aug. 2009), pp. 442–453. ISSN: 01968092. DOI: 10.1002/lsm.20782.

[55] Dmitry Yudovsky and Anthony J. Durkin. "Spatial frequency domain spectroscopy of two layer media". In: *Journal of biomedical optics* 16.10 (2011), p. 107005. ISSN: 1560-2281. DOI: 10.1117/1.3640814. URL: https://pubmed.ncbi.nlm.nih.gov/22029367/.

[56] Judi T. Whitton and J. D. Everall. "The thickness of the epidermis". In: *The British journal of dermatology* 89.5 (1973), pp. 467–476. ISSN: 0007-0963. DOI: 10.1111/J.1365-2133.1973.TB03007.X. URL: https://pubmed.ncbi.nlm.nih.gov/4753709/.

[57] Martin Johannes Koehler, Tanja Vogel, Peter Elsner, Karsten König, Rainer Bückle, and Martin Kaatz. "In vivo measurement of the human epidermal thickness in different localizations by multiphoton laser tomography". In: *Skin Research and Technology* 16.3 (Aug. 2010), pp. 259–264. ISSN: 1600-0846. DOI: 10.1111/J.1600-0846.2010.00437.X.

[58] John C Schotland, John C Haselgrove, and John S Leigh. "Photon hitting density". In: *Applied Optics* 32.4 (Feb. 1993), pp. 448–453. DOI: 10.1364/AO.32.000448. URL: https://opg.optica.org/ao/abstract.cfm?URI=ao-32-4-448.

[59] Luigi Belcastro, Hadi Shahin, Ahmed El-Serafy, Hanna Jonasson, and Rolf B. Saager. "Multi-frequency SFDI: inverse solving algorithm to reconstruct depth-resolved scattering properties in burn wounds ex-vivo." In: *Manuscript* (2023).

[60] Sean Thomas Horan. "Spectral Methods For Solving the Radiative Transport Equation in Single and Double Spherical Harmonics and Their Application to Optical Imaging". PhD thesis. UC Irvine, 2020.

[61] Stephen C Kanick, David M McClatchy, Venkataramanan Krishnaswamy, Jonathan T. Elliott, Keith D Paulsen, and Brian W Pogue. "Sub-diffusive scattering parameter maps recovered using wide-field high-frequency structured light imaging". In: *Biomedical Optics Express* 5.10 (2014), p. 3376. ISSN: 2156-7085. DOI: 10.1364/boe.5.003376.

[62] David M McClatchy, Venkataramanan Krishnaswamy, Stephen C Kanick, Jonathan T. Elliott, Wendy A Wells, Richard J. Barth, Keith D Paulsen, and Brian W Pogue. "High spatial frequency structured light imaging for intraoperative breast tumor margin assessment". In: *Advanced Biomedical and Clinical Diagnostic and Surgical Guidance Systems XIII* 9313.March 2015 (2015), p. 931308. DOI: 10.1117/12.2080134.

[63] Anouk L. Post, Dirk J. Faber, Henricus J. C. M. Sterenborg, and Ton G. van Leeuwen. "Subdiffuse scattering and absorption model for single fiber reflectance spectroscopy". In: *Biomedical Optics Express* 11.11 (Nov. 2020), p. 6620. ISSN: 2156-7085. DOI: 10.1364/boe.402466. URL: https://doi.org/10.1364/BOE.402466.

Papers

The papers associated with this thesis have been removed for copyright reasons. For more details about these see:

https://doi.org/10.3384/9789180753562

FACULTY OF SCIENCE AND ENGINEERING

Linköping Studies in Science and Technology, Dissertation No. 2347, 2023
Department of Biomedical Engineering

Linköping University
SE-581 83 Linköping, Sweden

www.liu.se